

# **Understanding the nanoscale structure of hexagonal phase lyotropic liquid crystal membranes**

Benjamin J. Coscia,<sup>†</sup> Richard D. Noble,<sup>†</sup> Douglas L. Gin,<sup>†,‡</sup> Joe Yelk,<sup>¶</sup> Matthew A. Glaser,<sup>¶</sup> Xunda Feng,<sup>§</sup> and Michael R. Shirts<sup>\*,†</sup>

<sup>†</sup>*Department of Chemical and Biological Engineering, University of Colorado Boulder,  
Boulder, CO 80309, USA*

<sup>‡</sup>*Department of Chemistry and Biochemistry, University of Colorado Boulder, Boulder CO  
80309, USA*

<sup>¶</sup>*Department of Physics, University of Colorado Boulder, Boulder CO, 80309, USA*

<sup>§</sup>*Department of Chemical and Environmental Engineering, Yale University, New Haven,  
Connecticut 06511, USA*

E-mail: michael.shirts@colorado.edu

## Abstract

Nanostructured porous membranes made from the cross-linked hexagonal phase of self-assembled lyotropic liquid crystals (LLCs) are a promising material for selective separations. In this work, we investigate an experimentally characterized LLC membrane using an atomistic molecular model. We use simulated X-ray diffraction (XRD) patterns in order to ensure maximum consistency between our structures and experiment. We show that pores are likely composed of 5 columns of stacked LLC monomers which surround each hydrophilic core. Although this system has been reported as dry, we show that small amounts of water are necessary to fully reproduce the experimental XRD pattern due to asymmetries introduced by hydrogen bonds between monomer head groups and water molecules. We explore the composition and structure of the nanopores and reveal that there exists a composition gradient rather than a abrupt partition between the hydrophilic and hydrophobic regions. A caveat is that the time scales of the dynamics are extremely long for this system, requiring starting from a range of alternative initial configurations and careful examination of the metastable states observed. The clearer picture of the nanoscopic structure of these membranes provided in this study will enable a better understanding of the mechanisms of small molecule transport within these nanopores.

## 1 Introduction

More highly selective membranes would be extremely useful for the recovery of dissolved species in complex aqueous and organic solutions. For example, selective membranes can further progress forward osmosis processes by reducing the cost of separating potable water from draw solutions.<sup>1</sup> Additionally, flowback water (FW) produced during hydraulic fracturing is a complex wastewater full of potentially valuable dissolved organic compounds such as acetate that can be recovered using highly selective membranes.<sup>2</sup> Finally, a significant amount of nitrogen and phosphorus from fertilizer is found in wastewater. Selective mem-

branes offer a route towards low energy nutrient recovery from these wastewaters which can help sustain fertilizer production and subsequently food production into the future.<sup>3</sup>

Current commercial RO and NF membranes suffer limitations to their selectivity because they are unstructured. Although scalable, their fabrication involves the spontaneous assembly of polymers into disordered structures which offer separation pathways that are tortuous and polydisperse in size. This makes overcoming the well-known permeability-selectivity tradeoff a challenge. Namely, it is difficult to increase the permeability of a desired molecular or atomic species, while maintaining the same retention of an undesired species.<sup>4</sup>

Selective separation by a semipermeable membrane barrier is a function of the geometric and chemical interactions of solutes with the membrane material. A molecule's size, shape, charge and polarity combine to determine the degree to which a solute partitions into a membrane and how fast it travels through the membrane. To separate a component from a mixture, one must understand how to design membranes in order to tune the relative transport rates of desired and undesired solutes.<sup>5,6</sup>

Preliminary evidence has shown that crosslinked lyotropic liquid crystal (LLC) membranes may be capable of performing highly selective separations. LLCs are amphiphilic molecules that have the ability to self-assemble into porous nanostructures<sup>7</sup> and can be crosslinked to create mechanically strong membrane films with pores on the order of 1 nm in diameter.<sup>8</sup> Unlike most commercial NF membranes, LLC membrane pores are uniform in size because they are self-assembled. Since LLC membranes lack a pore size distribution, they inherently exhibit high selectivity due to their strict molecular weight cut-off (MWCO).<sup>8</sup> Additionally, the LLC monomers examined in this paper are salts, and therefore lead to Donnan exclusion of ions in solution. The membrane gains a net surface charge when counterions from the head groups that line the pore walls escape into the feed solution in an effort to balance the gradients of concentration and electric potential.<sup>9</sup>

The feasibility of nanostructured LLC membranes for selective separations has been demonstrated using LLCs that form the type 1 bicontinuous cubic ( $Q_1$ ),<sup>10-12</sup> and the in-

verted hexagonal ( $H_{II}$ )<sup>8</sup> phases. When separating organic solutes from NaCl,  $Q_I$  phase membrane filtration experiments have shown selectivity 2–3 times higher than commercial RO and 6–12 times higher than commercial NF membranes.<sup>2</sup> When separating a series of various sized dyes, the  $H_{II}$  phase membrane showed complete rejection of dyes bigger than 1.2 nm in size.<sup>8</sup>

The  $H_{II}$  phase pore geometry has a higher theoretical capacity for transport than the  $Q_I$  phase. The  $H_{II}$  phase forms at room temperature in the presence of c.a. 10 wt% water and consists of hexagonally packed, hydrophilic pore columns.<sup>7</sup> In the absence of water, neat monomer will form the same hexagonal columnar structure which, in literature, has been referred to as the  $Col_h$  thermotropic phase.<sup>13</sup>  $Q_I$  phase membranes consist of a tortuous network of three dimensionally interconnected pores that prevent optimal through-plane transport. The densely packed, non-tortuous and uniform sized pores of  $H_{II}$  phase membranes represent the ideal geometry for achieving high solute flux.<sup>14</sup> Despite the promise of the  $H_{II}$  phase, the hexagonally packed liquid crystalline domains, formed when monomers self-assemble, are isotropically aligned which is detrimental to membrane permeability.

Recently, researchers have learned how to macroscopically align the hexagonal domains which has revived research into  $H_{II}$  phase LLC membranes. Previously, research efforts were focused on the  $Q_I$  phase, whose geometry does not require alignment. In 2014, Feng et al. showed that one can align  $Col_h$  hexagonal domains, created by the monomer Na-GA3C11, using a magnetic field with subsequent cross-linking to lock the structure in place.<sup>13</sup> In 2016, Feng et al. showed that one could obtain the same result by confining neat monomer between PDMS or glass substrates since hexagonal mesophases preferentially anchor perpendicular to both surfaces.<sup>15</sup> Current experimental efforts are focused on extending the method to the  $H_{II}$  phase and characterizing the performance of these newly aligned systems.

Our current understanding of the molecular details of LLC membranes' nanostructure is not sufficient to be able to precisely design them for specific separations. Over the past 20 years,  $H_{II}$ -phase LLC polymer membrane studies have been limited primarily to Na-GA3C11

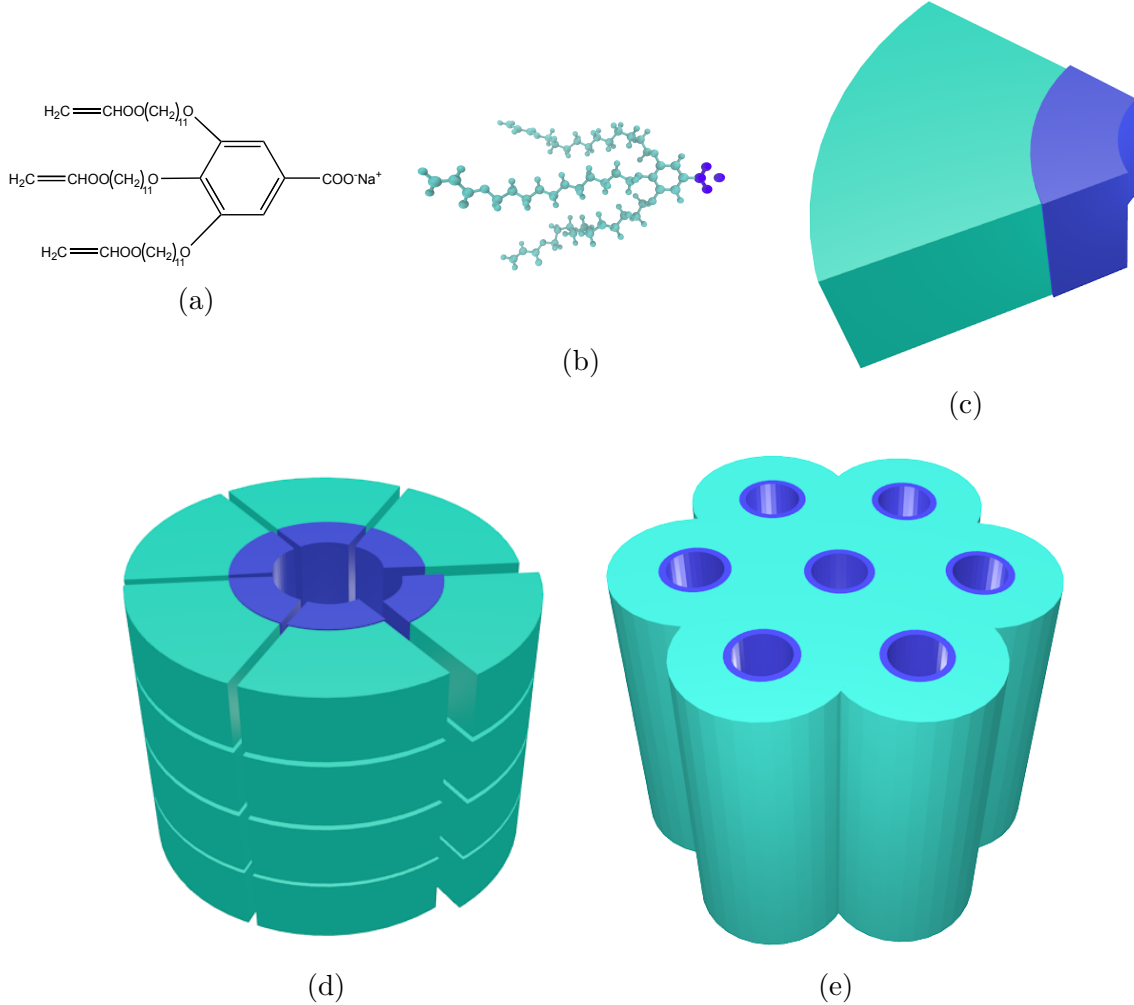


Figure 1: (a) The LLC monomer Na-GA3C11 (b) rendered atomistically (c) exhibits wedge-like character. (d) Monomers stack on top of each other with short range order and assemble into pores. (e) The hydrophilic head groups (blue) facing towards the pore center. The pores assemble into hexagonally packed columnar mesophases.

with some characterization done after minor structural modifications. Resel et al. varied the length of the monomer tails and the counterion used and observed its effect on pore spacing.<sup>16</sup> In a later study of rejection performance, it was shown that membranes formed by cross-linked Na-GA3C11 in the H<sub>II</sub> phase cannot separate solutes less than 1.2 nm in diameter because the pores are too large.<sup>8</sup> We do not yet understand how to controllably reduce the effective pore size or how to tune the chemical environment in the nanopores of this or related materials for small molecule separations. The only source of predictive modeling for LLC systems have been macroscopic models that likely do not adequately describe transport at these length scales.<sup>10</sup> Modeling with molecular detail could provide sufficient information about the mechanisms and chemical features to better inform experimental design of similar nanostructured membranes.

A molecular-level understanding of LLC membrane structure, enabled by molecular dynamics (MD) simulations, can provide guidelines to reduce the large chemical space available to design monomers for creation of separation-specific membranes. Useful molecular-level modeling should incorporate a detailed picture of the nanoscopic pore structure which is crucial to understanding the role of monomer structure in solute transport and membrane design. Atomistic molecular dynamics simulations can provide the required level of detail (Figure 2), assuming the force fields are sufficiently accurate. With such an atomistic model, we can directly observe molecular-level solute transport and suggest governing mechanisms. We can observe how the choice of head group interacts with solutes of interest. We can interchange counterions which may influence both the pore size and the strength of the Donnan potential.

In this study, we achieve a more realistic atomistic description of LLC membranes than, to our knowledge, has ever previously been created, and explore what new structural information can be gained and what structure hypotheses are supported by this model. We validate the results using as much experimental information as possible. We are most interested in reproducing the conclusions about structure drawn from small angle X-ray scattering

(SAXS) and wide angle X-ray scattering (WAXS) experiments as well as in matching ionic conductivity measurements.<sup>15</sup>

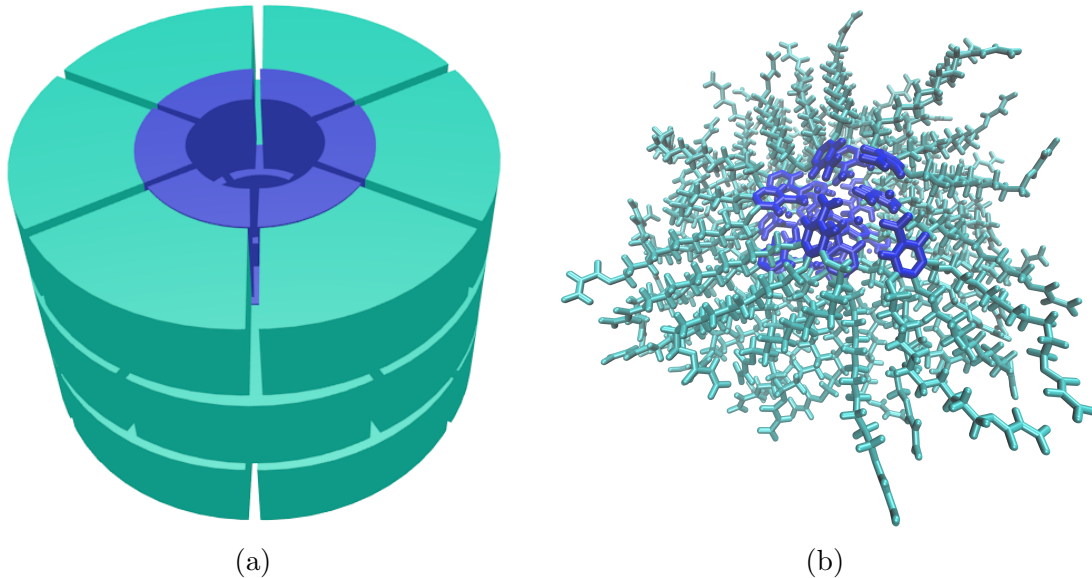


Figure 2: (a) Previous understanding of the pores are essentially speculations based on limited chemical and experimental data. (b) We use detailed molecular modeling in this paper in order to appropriately model the pore’s complex architecture which is crucial to understanding the mechanism of solute transport. In both pictures, the head group region is colored blue and the tail region is colored cyan.

In this paper, we perform molecular modeling of the Col<sub>h</sub> assembly formed by Na-GA3C11. Compared to the H<sub>II</sub> phase, the Col<sub>h</sub> phase is a simpler starting point. The system is not assembled in aqueous phase which allowed us to simulate longer timescales, and there exists detailed experimental characterization of the fully aligned state, including 2D wide-angle X-ray scattering (WAXS) patterns (Figure 3b) which are useful for reconstructing structural data.

There are five major features of interest present in the 2D experimental pattern shown in Figure 3b.

1.  $R\text{-}\pi$ : The location of the first is at  $q_z = 1.7 \text{ \AA}^{-1}$ , corresponding to a real space separation of 3.7 Å. Previous work<sup>13</sup> attributes this reflection to  $\pi\text{-}\pi$  stacking between aromatic

rings in the direction perpendicular to the membrane plane, or z-axis.<sup>13</sup> For simplicity, we will refer to this reflection as R- $\pi$ .

2. *R-double*: A weak intensity line, located at exactly half the  $q_z$  value of R- $\pi$  ( $q_z = 0.85 \text{ \AA}^{-1}$ ), corresponds to real space periodicity of 7.4 Å. Since this reflection corresponds to double the spacing of R- $\pi$  in real space, we will refer to this reflection as R-double. R-double has been interpreted as  $2_1$  helical ordering of aromatic rings along the  $z$  axis,<sup>13</sup> meaning that if one traces the positions of the aromatic rings with a helical curve, then for each full turn in the helix, one will encounter two aromatic rings.
3. *R-alkanes*: A low intensity ring located at  $r = 1.4 \text{ \AA}^{-1}$  marks the third major reflection of interest. The real space separation corresponds to 4.5 Å which is characteristic of the average spacing between packed alkane chains.<sup>17</sup> We will call this reflection R-alkanes.
4. *R-spots*: Within R-alkanes, are four spots of higher relative intensity. Accordingly, we name these reflections R-spots. The location of all spots is  $\sim 37^\circ$  from the  $q_z$  axis in their respective quadrants. In many liquid crystal systems one can explain the spots as the product of alkane chains tilted with respect to the membrane plane.<sup>18</sup>
5. *R-pores*: The final feature corresponds to the spacing and symmetry of the  $d_{100}$  plane. This plane is geometrically related the distance between pores. The feature, which we named R-pores, is characterized by dots along the equatorial axis defined by  $q_z = 0$ . The spacing between dots is indicative of the hexagonal symmetry of the packed pores. We observe the same information with higher resolution using SAXS (Fig. 3a).

Despite having structural data, there is still information which experiment cannot definitively answer. Specifically, we want to know:

1. What is the density of monomers that pack around each hydrophilic core?

Authors often describe this and similar systems as being made up of layers. A simple molecular simulation study of a similar molecule suggested that there are 4 monomers

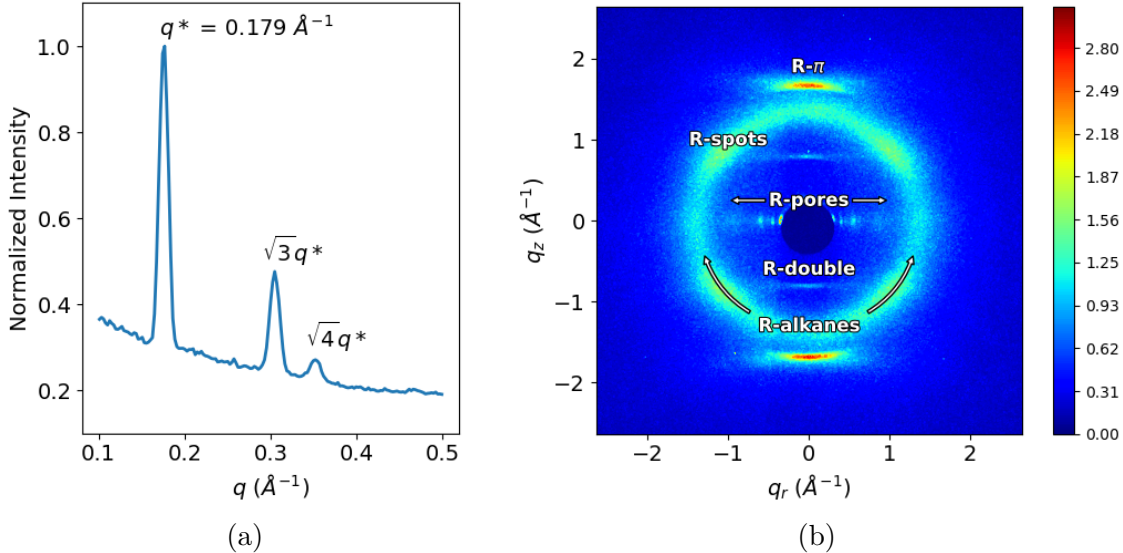


Figure 3: (a) (Reproduced from 15) The repeat spacing in the 1D small angle X-ray scattering pattern is characteristic of hexagonal packing. The leading peak,  $q^*$ , represents the distance between the  $d_{100}$  planes. Using this distance, we know that the distance between pore centers is 4.12 nm. (b) 2D WAXS gives details about repeating features on the order of angstroms. Experimentalists have explained each of the 5 major reflections present as follows: (R- $\pi$ ) Aromatic head groups  $\pi - \pi$  stack 3.7 Å apart. (R-double) Monomers arrange vertically in a  $2_1$  helix. (R-alkanes) Alkane chain tails pack 4.5 Å apart. (R-spots) Monomer tails are tilted with respect to the membrane plane. (V) As derived from SAXS, the pores are spaced 4.12 nm apart and pack hexagonally

in each layer. Their estimation is based on a simulated system containing only 16 total monomers which likely does not sufficiently model the chemical environment present in the real system.<sup>19</sup> A separate calculation based on the volume of the liquid crystal monomers proposes that there are seven monomers in each layer.<sup>16</sup>

We are careful to avoid the term 'layers' since many liquid crystalline systems have long range order in 1 or 2 spatial dimensions and short range order in the other dimensions.<sup>20</sup> In the system we are studying, there are long-range 2D correlations in the hexagonal array of pores (xy plane) and short range z-direction correlations between stacked columns of monomers. In this study, we use atomistic molecular modeling to study how the system's structure is affected by the density of these monomer columns that surround each pore's hydrophilic core.

## 2. What structural motif best matches experimental 2D WAXS patterns?

On the short timescales accessible to MD (even the 100's of nanoseconds of simulation performed here are short compared to experimental timescales), we observe distinct metastable configurations which depend on starting configuration. We simulated XRD patterns of our system and compared them to experimental 2D WAXS patterns (Figure 3b) so that we ensure our model creates a nanoscopic chemical environment maximally consistent with experiment within the constraints of our forcefield. Using this approach, we are able to confirm some previous interpretations of the WAXS pattern and refute others.

## 3. Is it necessary to include any water in order to appropriately model the Col<sub>h</sub> phase?

While the Col<sub>h</sub> phase is described as dry, it is likely that small amounts of ambient water are absorbed into the system. The hydrogen bonding network formed by the water may play a role in structuring the pore. We used simulated X-ray diffraction (XRD) patterns to see if there is any meaningful structural difference between a "dry" and a "wet" system.

## 4. What is the detailed atomistic structure of the pores?

The limited picture that experiment provides tells us that there are hexagonally packed, hydrophilic regions where transport is likely to occur. One may instinctively imagine these regions as tube-like pathways with well-defined boundaries. We explored the composition of the pores, the partition between the hydrophilic and hydrophobic regions, and its sensitivity to initial configuration, including both dry and wet systems.

## 2 Methods

### 2.1 Monomer Parameterization

We parameterized the liquid crystal monomer Na-GA3C11 using the Generalized AMBER Force Field (GAFF)<sup>21</sup> with the Antechamber package<sup>22</sup> provided with AmberTools16.<sup>23</sup> We assigned atomic charges using the am1bccsym method of `molcharge` shipped with QUACPAC from Openeye Scientific Software. We ran all molecular dynamics simulations using GROMACS 2016.<sup>24-27</sup>

We generated an ensemble of characteristic, low-energy vacuum monomer configurations by applying a simulated annealing process to a parameterized monomer. We cooled monomers from 1000K to 50K over 10 nanoseconds. We randomly pulled a low energy configuration from the trajectory then reassigned charges using `molcharge`. Using the new charges, we annealed the monomer system again and pulled a random monomer configuration from the trajectory which we used for full system construction (Figure 4a). See section S-2 for further detail of the parameterization process.

### 2.2 Unit Cell Preparation

The timescale for self-assembly of monomers into the hexagonal phase is unknown and likely outside of a reasonable length for an atomistic simulation, calling for a more efficient way to build the system. Previous work has shown a coarse-grained model self assemble into the H<sub>II</sub> phase configuration in  $\sim$ 1000 ns.<sup>28</sup> We attempted atomistic self-assembly by packing monomers into a box using Packmol.<sup>29</sup> Simulations of greater than 100 ns show no indicators of progress towards an ordered system (see section S-1). To bypass the slow self-assembly process, we use Python scripts to assemble monomers into a structure close to one of a number of hypothesized equilibrium configurations (Figure 4).

A typical simulation volume contains four pores in a monoclinic unit cell, the smallest unit cell that maintains hexagonal symmetry when extended periodically. Each pore is made

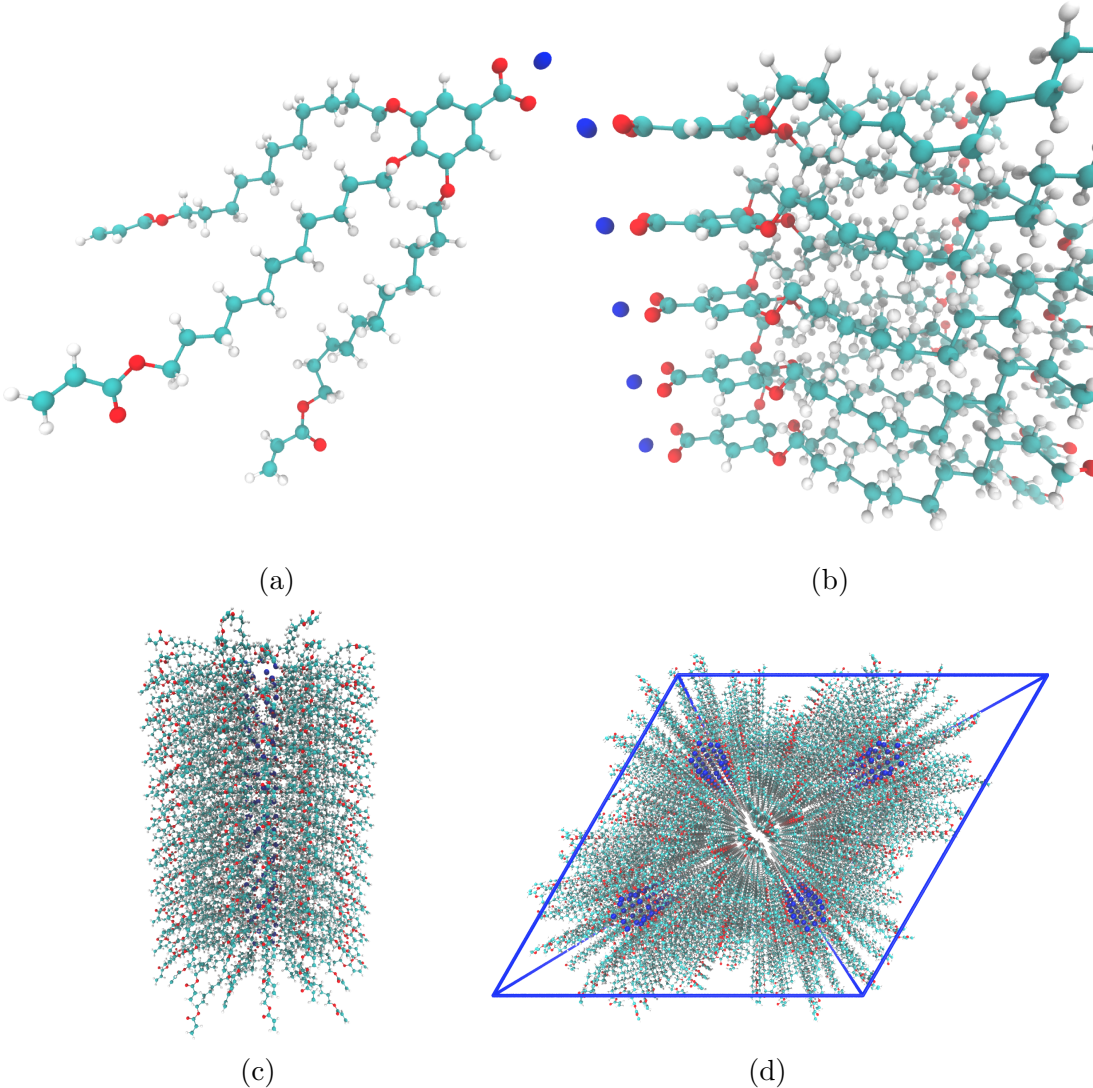


Figure 4: (a) We parameterized a single monomer and annealed it to produce a low energy configuration. (b) We assembled monomers into columns by stacking them on top of each other. (c) We duplicated each column and rotated them to create hydrophilic pore centers. We chose to stack twenty monomers into each column. (d) We duplicated the pores and placed them into a monoclinic unit cell.

of columns of stacked monomers with periodic continuity along the pore axis, avoiding any edge effects and creating an infinite length pore ideal for studying transport. We prefer a small number of stacked monomers in order to reduce computational cost and to allow us to look at longer timescales. Ultimately, we chose to build a system with 20 monomers per column in order to minimize finite size effects with reasonable computational expense and to

obtain sufficient resolution when simulating XRD patterns (see further discussion in section S-3).

## 2.3 Monomer Placement

When constructing an initial configuration, there are a number of variables which require careful consideration while placing monomers. The equilibrium configuration is sensitive to some while insensitive to others. We find the starting pore radius, defined as the distance of a chosen head group carbon from the pore's central axis, does not influence the equilibrium structure if one chooses a reasonable value. The pore radius is chosen to be 0.5 nm in our initial configurations. The initial distance between pores, within a wide range, also has little effect on the the equilibrated structure. However, one should not start them too close or there will be high energy repulsions during early equilibration. We chose an initial pore spacing of 4.5 nm,  $\sim$ 10% larger than the experimental value of 4.12 nm. A sensitivity analysis of both parameters is presented in the Supporting information, section S-4. The distance between vertically stacked monomers, the xy position of monomers with respect to vertically adjacent monomers, and the number of columns per pore do influence the equilibrated structure and require further justification for their choices. We rely on experimental data to inform them.

We chose the vertical spacing between monomers for the initial configuration based on  $R-\pi$  and then allowed the system to readjust during equilibration. We rotated each monomer so the plane of its aromatic head group would be coplanar with the xy plane. We explored three different initial monomer spacings. The first is exactly equal to  $R-\pi$  with layers placed so aromatic rings stack 3.7 Å apart in the z-direction. We explore a second system with an initial spacing of 5 Å. We briefly explored a third system with an initial spacing of 10 Å. However this spacing yields non-physical behavior which is detailed in the Supporting Information, section S-4.3.

We chose the relative orientation between vertically adjacent monomers in each column based on clues from diffraction data as well as the various known stacking modes of benzene

and substituted benzene rings: sandwiched, parallel-displaced and T-shaped.<sup>30</sup> We ruled out the T-shaped configuration because its  $\sim 5 \text{ \AA}$  equilibrium stacking distance<sup>30</sup> is inconsistent with  $R-\pi$ . It is also infeasible for the monomers to orient in the T-shaped conformation because of the bulky tail groups. We explored the system's preference towards the sandwiched vs. parallel displaced stacking modes in some detail. Both have reported stacking distances near the  $R-\pi$  value of  $3.7 \text{ \AA}$ . Head groups in our sandwiched initial configuration stack directly on top of each other while head groups in the parallel displaced initial configuration stack with an offset of  $180^\circ / n_{\text{col}}$  where  $n_{\text{col}}$  is the number of columns per pore. See Figure S-5 for a detailed illustration of the initial configurations in each mode.

The number of columns per pore is unknown, as stated in question (1). We tested configurations constructed with a varied number of columns per pore. We built systems in the sandwiched and parallel displaced configurations with 4, 5, 6, 7 and 8 monomers per layer.

## 2.4 Equilibration

We developed equilibration schemes for creating dry and wet configurations. Both schemes start with an initial configuration generated according to the previous guidelines. For wet systems, we added the desired concentration of water to the initial configuration and carried out equilibration in the same way as the dry systems. First, we fixed monomer head groups in place using position restraints with a force constant of  $10^6 \text{ kJ mol}^{-1} \text{ nm}^{-2}$ . We gradually released the position restraints by decreasing the force constants over a series of NVT simulations. We allowed the resulting unrestrained structure to equilibrate for 5 ns in the NPT ensemble with pressure controlled by the berendsen barostat followed by NPT equilibration simulations run for at least 400 ns using the Parrinello-Rahman barostat. More equilibration details are available in section S-5.

## 2.5 Equilibrium Calculations

### 2.5.1 Determining equilibration time

Using equilibrated structures, we carried out various calculations to characterize the system. We defined the point at which a system is equilibrated based on when the distance between pores stopped changing. We determined when the distances stopped changing by applying the statistical test, `pymbar.timeseries.detectEquilibration`, to the time series.<sup>31,32</sup> Typically, the pore-to-pore distance equilibrated between 200 and 350 ns. We used data collected after equilibration to do all subsequent analysis.

### 2.5.2 Calculation of pore spacing

To calculate the equilibrated pore spacing, we measured the distance between pore centers. We located the pore centers by averaging the coordinates of sodium ions in their respective pores. We generated pore spacing statistics using the bootstrapping technique (See section S-6 of the Supporting Information).

### 2.5.3 Pair distribution functions and correlation length

The normalized pair distribution function,  $g(\mathbf{r})$ , describes the probability of finding a pair of particles separated by  $\mathbf{r}$ ,

$$g(\mathbf{r}) = \frac{1}{\rho N} \left\langle \sum_{i=1}^N \sum_{j \neq i}^N \delta(\mathbf{r} + \mathbf{r}_j - \mathbf{r}_i) \right\rangle \quad (1)$$

where  $\rho$  is the average number density of particles and  $\delta(\mathbf{r})$  is the Dirac delta function.<sup>33</sup> We applied equation 1 in three dimensions and then extracted one dimensional distribution functions using slices of the grid along the appropriate axis.

We measured the one dimensional pair distribution function,  $g(z)$ , between centers of masses of aromatic head group rings along the z-axis (perpendicular to the membrane plane). We averaged all 1D slices in the z-direction of the full 3D correlation function within 2.1 Å of

$(x, y) = (0, 0)$ . We chose 2.1 Å as a crude approximation of the radius of the phenyl ring plane. We calculated the radius as the sum of the longest C-C distance within a phenyl ring (2.8 Å) and two times the carbon atom radius (0.7 Å).

Here,  $g(z)$  is characterized by an oscillatory function with a period equal to the average distance between stacked monomers, and an amplitude that decays exponentially (see Figure 10). The rate of decay is related to the correlation length, L, between monomer head groups. We estimated L by fitting the peaks of  $g(z)$  to a decaying exponential function of the form:

$$Ae^{-z/L} \quad (2)$$

where A is a fitting parameter for amplitude, z is the independent variable of  $g(z)$  and L is the fit correlation length. We calculated the error in the estimated value of L as the square root of the diagonal entry of the covariance matrix of optimized fit parameters.

We also used  $g(z)$  to calculate the equilibrated vertical stacking distance between monomers,  $d_{equil}$ . We fit a decaying sinusoidal function to  $g(z)$  of the form:

$$1 - A \cos\left(\frac{2\pi}{d_{equil}}z + B\right) e^{-z/L} \quad (3)$$

where A and B are fit parameters for the function's amplitude and phase shift respectively. This function could be used in place of Equation 2, however it does not consistently fit the peaks of  $g(z)$  from parallel displaced configurations well enough to extract a reliable value of L.

#### 2.5.4 *Radial distribution functions*

We explored the pores' compositions by measuring the average number densities of various monomer components as a function of distance from the pore centers. We looked at the average number density of sodium ions, aromatic rings and carbon atoms making up the monomer tails. We binned the radial distance of all atoms in each group from the pore

centers, then normalized by the volume of the annulus defined by the bin edges and the z box vector (See Figure S-20).

### 2.5.5 *Simulated structure factor calculations*

We generated simulated XRD patterns based on atomic coordinates in order to make a direct experimental comparison. We modeled all atomic coordinates as Gaussian spheres of electron density corresponding to each atom's electronic radius. A three dimensional Fourier transform (FT) of the array of electron density results in a three dimensional structure factor which represents the unit cell in reciprocal space. The experimental WAXS measurement was made using a vertically aligned film whose pores were oriented perpendicular to the direction of the incident X-ray beam. Although the pores were vertically aligned, the crystalline domains were still misaligned with respect to the xy plane. To account for this, we averaged 2D slices of the structure factor at all angles about  $|\mathbf{q}| = (0, 0, z)$ .

We normalized all diffraction patterns relative to R-alkanes. We believe that the alkane-alkane density, averaged over all angles, is the feature most likely to be replicated between experiment and simulation, as atomistic alkane parameters are relatively well studied. Other features are dependent on system ordering which is likely to have some dependence on initial configuration. We calculated the average intensity within R-alkanes of the experimental pattern,  $I_{avg}$  and divided all intensities by this value. In this way, the average intensity of R-alkanes was equal to 1. When calculating  $I_{avg}$ , we excluded intensities within  $\pm 30^\circ$  of the meridional axis defined by  $q_r = 0$ , since the simulated patterns differ from experiment in those regions in all cases. Specifically, in contrast to the experimental WAXS pattern, R- $\pi$ , as it appears in the simulated diffraction patterns, intersects with R-alkanes (See Figure 6). We set an upper bound on the colorbar by multiplying  $I_{avg}$  by a scaling factor,  $f$ . Intensities that appear in the patterns  $\geq f \times I_{avg}$  are colored uniformly. We applied the same scaling method to the simulated patterns. We carefully chose a scaling factor of  $f = 3.1$  in order to visibly display all features in all patterns.

### 2.5.6 Ionic conductivity calculations

We calculated ionic conductivity using the Nernst-Einstein relationship, which relates the DC ionic conductivity,  $\sigma$ , to ion diffusivity,  $D$ , concentration,  $C$ , ion charge,  $q$ , the Boltzmann constant,  $k_b$ , and temperature,  $T$ :

$$\sigma = \frac{q^2 C D}{k_b T} \quad (4)$$

We measured sodium ion diffusion coefficients by calculating the slope of the linear region of the z-direction mean square displacement curve as indicated by the Einstein relation.<sup>34</sup> We visualized the MSD plot to determine where to begin and end a linear fit. We measured ion concentration with respect to the volume of the entire unit cell. More details are provided in the Supporting Information, Section S-14.

## 2.6 Cross-linking

In order to maximally match the experimental membrane synthesis process, we created a cross-linking algorithm that one can apply to equilibrated structures. The primary purpose of cross-linking is to create a mechanically robust membrane. For that reason, we are not concerned with replicating the kinetics of the reaction, but instead emphasize understanding how much and in what way cross-linking modulates the system's structure.

We based our cross-linking algorithm on the known reaction mechanism (Figure S-25). The reaction takes place at the terminal vinyl groups on each alkane tail. The procedure is carried out iteratively. Each iteration, the algorithm chooses carbons to cross-link based on the distance between eligible carbon pairs. The algorithm then updates the topology with the new bonds and atom types, energy minimizes the system and runs a short simulation before selecting the next group of eligible carbons atoms.

## 3 Results and Discussion

### 3.1 Density of monomers around pores

Our simulations best support a model built with 5 monomer columns per pore based on the measured equilibrated pore-to-pore distances. To discern the composition of the monomer layers, addressing question 1 above, we ran simulations of systems created with 4–8 columns per pore. We built systems in both the parallel displaced and sandwiched configurations and equilibrated them according to the dry equilibration procedure. We tested all systems with an initial vertical monomer spacing,  $d$ , of 3.7 Å in accordance with R- $\pi$ . We tested 4 additional systems with monomers initially spaced 5 Å apart vertically (see section 4.1 of the Supporting Information for more details on sensitivity to initial layer spacing). We considered the pore-to-pore spacing to be equilibrated as defined in section 2.5.1. Figure 5 shows the equilibrated pore-to-pore distances for all systems tested.

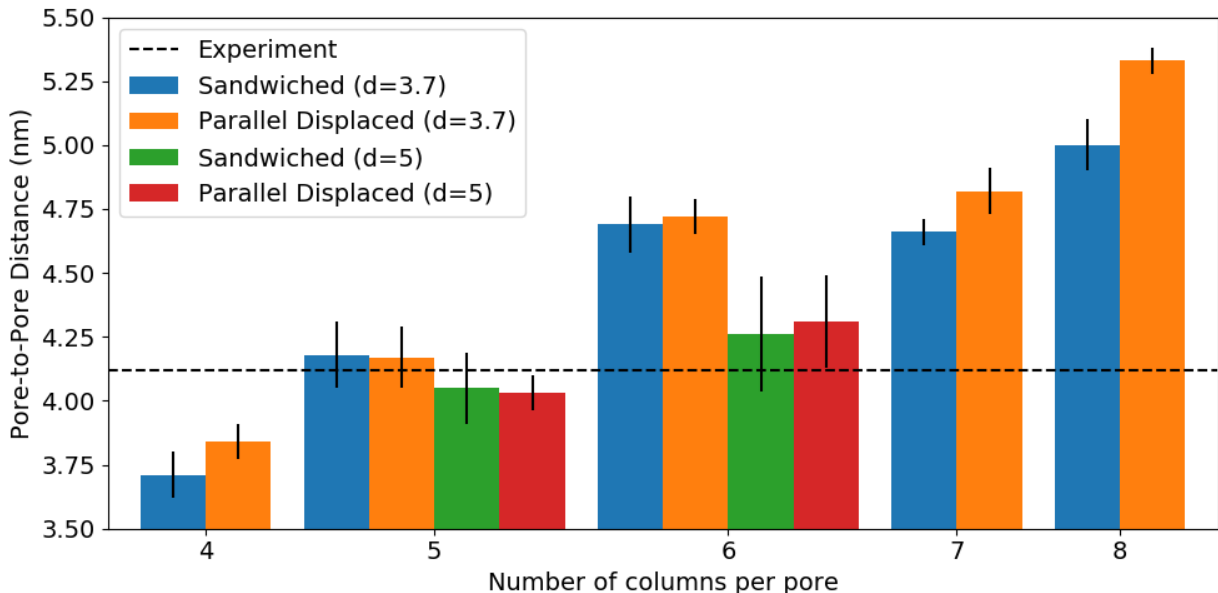


Figure 5: Systems with 5 columns per pore have equilibrated pore spacings closest to the experimental value of 4.12 nm. The equilibrated pore spacing of the model increases as the number of columns in each pore increases.

All systems tested, although equilibrated from the perspective of the metrics used here,

are frozen in metastable basins. Not all make physical sense or fit the experimental profile that we are trying to match. In the limit of infinite simulation time, all systems will in theory converge to a single equilibrium configuration, but that time is far beyond the 100's of nanosecond simulated here. For simplicity, we group the systems studied here into the ordered and disordered basins. What we find is that any system where  $d = 3.7 \text{ \AA}$  can generally be characterized as being in a more ordered basin, and any system where  $d = 5.0 \text{ \AA}$  can be characterized as a more the disordered basin. Generally, when monomers are started further apart, they stay further apart than systems where monomers are started closer together (see Table 3). Because of the extra space between stacked monomers, monomer head groups have more rotational freedom. We quantified the ordering of the head groups using the nematic order parameter (see section S-7 for details of calculation). Disordered basin systems have a lower nematic order parameter (meaning they are more disordered) than ordered basin systems.

Systems built with 5 columns in each pore equilibrate to a pore spacing that is most consistent with the experimental value of 4.12 nm derived from SAXS measurements (Figure 3a). Ordered basin systems built with 4 columns per pore equilibrate to an average pore spacing 0.25 nm lower than experiment. Ordered basin systems built with 6 columns per pore, have an equilibrated pore spacing ca. 0.50 nm higher than experiment. Monomers in disordered basin systems built with 6 columns-per-pore agree with experimental pore-to-pore distances within error, but stack too far apart. Those in the disordered sandwiched and disordered parallel displaced configurations stack  $\sim 4.87$  and  $4.94 \text{ \AA}$  apart respectively, which is ca.  $1.2 \text{ \AA}$  further apart than suggested by experiment. 5 column-per-pore systems stack, at a maximum, 0.9  $\text{\AA}$  further apart than experiment (see Table 3). The remainder of this discussion will focus on the analysis of systems built with 5 columns per pore.

## 3.2 Simulated XRD comparison to 2D WAXS data

We further refined our structural understanding of the system by simulating X-ray diffraction patterns produced from equilibrated MD trajectories and comparing them to experiment. We tested systems built with 5 columns per pore in the parallel displaced and sandwiched configurations at 300 K in the ordered and disordered basins. We generated simulated patterns using the equilibrated portion of each simulation trajectory. The patterns for all structures are shown and compared to experiment in Figure 6.

The diffraction patterns show some noise, especially along the axis where  $q_r=0$ . There are two main reasons for this noise. First is that we angle averaged the 3D structure factor (see section 2.5.5) which inherently gives less data as  $q_r$  approaches 0. Second, our simulations are not long enough to sample enough truly independent configurations within their respective metastable basins. By sampling more uncorrelated equilibrium configurations, we can suppress some of the noise (See section S-9).

The simulated XRD patterns show moderate qualitative agreement with experiment. R-alkanes and R-pores appear in the expected location. R-pores is more intense than experiment, likely because we are simulating a near perfect, infinite hexagonal array. The real system has defects and domain misalignment which decreases the overall intensity. R-spots appears to be weaker, except for the ordered basin sandwiched configuration, in the simulated patterns. R-spots is also partially engulfed by the wide R- $\pi$  reflection. R- $\pi$  appears at a lower  $q_z$  value than experiment. In all systems, the reflection reaches its maximum at  $q_z < 1.5 \text{ \AA}^{-1}$  which means that monomers prefer to stack at least 4.2 Å apart rather than 3.7 Å. R-double does not appear in any of the patterns.

The simulated XRD patterns of the parallel displaced configurations show an additional reflection due to their helical structure. There are weak horizontal reflections near  $|q_z| = 0.7 \text{ \AA}^{-1}$ , half of the  $q_z$  value of R- $\pi$ . The reflection does not cross through  $q_r = 0 \text{ \AA}^{-1}$  so it does not necessarily appear for the same reason as R-double. This type of pattern is characteristic of a helix,<sup>35</sup> as the head groups in the parallel displaced configuration are

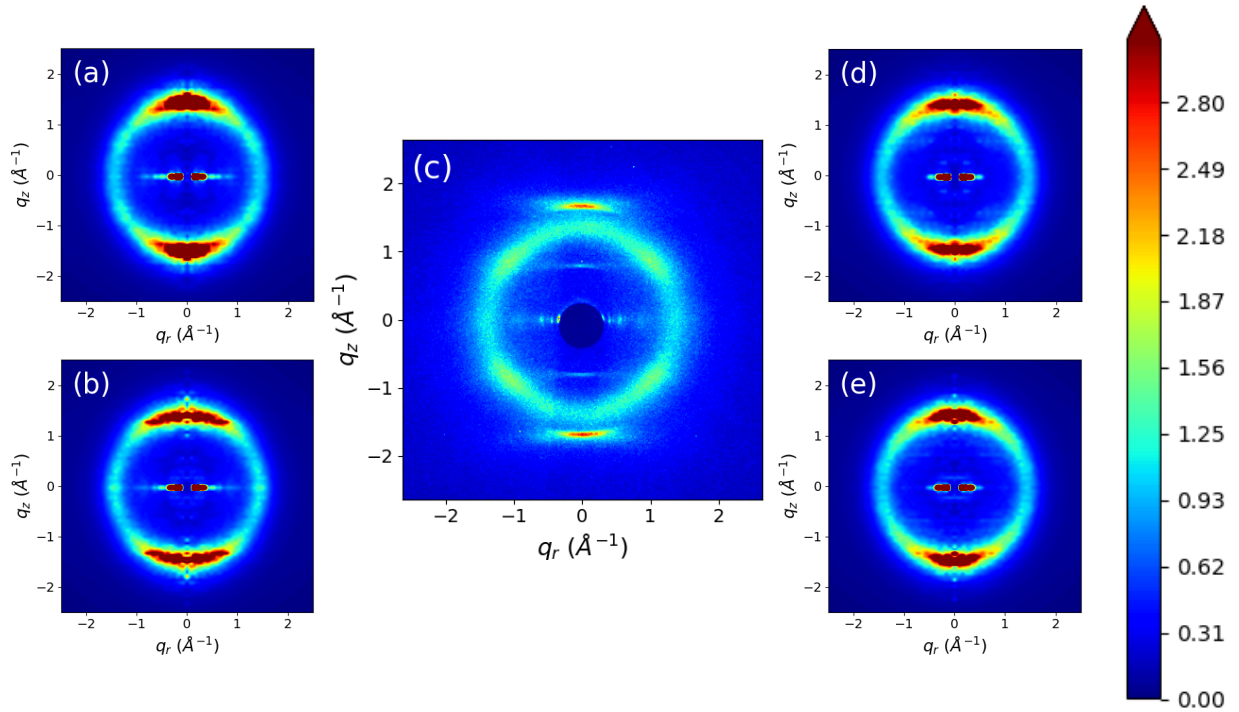


Figure 6: Simulated XRD patterns show some qualitative agreement with experiment. Shown is a comparison of the (a) Sandwiched, ordered basin (b) Sandwiched, disordered basin (d) Parallel displaced, ordered basin and (e) Parallel displaced, disordered basin configurations with (c) experimental WAXS. In all cases, R-pores, R-alkanes and R- $\pi$  are present to some degree. R-spots is also present, however it is generally partially covered by the broad R- $\pi$  reflection. Quantitative comparisons of the relative intensities of reflections of interest are presented in Table 1. In both XRD patterns generated from parallel displaced patterns, there is a faint line across  $q_z \sim 0.7 \text{ \AA}^{-1}$ , half the simulated value of R- $\pi$ . Although it does not cross through  $q_r = 0 \text{ \AA}^{-1}$ , it is at the same  $q_z$  value where we expect R-double to be present. Still, R-double is not fully reproduced in any of the simulated patterns.

arranged in a helix. It is possible that these reflections contribute to the diffuse reflections that connect R-spots and R-double in the experimental pattern.

We quantified the numerical discrepancies present when comparing the relative intensities of each reflection of interest between experimental and simulated patterns. Table 1 shows the relative intensities of each reflection for all systems tested. The patterns are normalized so that the average intensity of R-alkanes must equal 1. We measured the approximate intensity of R- $\pi$  and R-double by measuring the intensity of the appropriate peaks of the cross-section of the 2D pattern at  $q_r = 0$ . The relative intensity of R- $\pi$  is significantly higher

than experiment in our simulations. R-spots is measured as the average intensity within the region bounded by a 'spot'. We identified spots based on visual inspection. If the spots were not easily discernible, then the intensity was taken as that of the intersection of R-alkanes at half the  $q_z$  value of R- $\pi$ , since that is where it appears experimentally. The intensity of R-spots is slightly lower than experiment in all cases except for the ordered basin sandwiched configuration which agrees with experiment. There is no R-double intensity to be measured. Figures are provided in section S-8 to make these measurements clear.

**Table 1:** The simulated XRD patterns of the systems tested, normalized so that the average intensity of R-alkanes equals 1, show R- $\pi$  reflections that are significantly higher than experiment and R-spots reflections that are slightly lower than experiment. R-double does not appear in any patterns, and thus has no measurable intensity.

Reflection	Configuration					
	Experiment	Sandwiched	Parallel Displaced	Disordered Sandwiched	Disordered Parallel	Disordered Displaced
R-alkanes	1.0	1.0	1.0	1.0	1.0	1.0
R-spots	1.3	1.3	1.2	1.1	1.2	
R- $\pi$	2.8	44.0	7.7	8.4	10.1	
R-double	0.9	—	—	—	—	—

There are clear differences between simulated and experimental results that must be addressed and justified. We will explore the possible origin of select experimental reflections and form structural hypotheses related to their appearance in our simulated patterns. Specifically, we want answer:

1. What is the origin of R-spots?
2. Why is the intensity of R- $\pi$  so much greater than experiment?
3. What is the origin of R-double?

### 3.2.1 Origin of R-spots

In order to more clearly study R-spots, we equilibrated an ordered basin sandwiched configuration at 280K. Obtaining an equilibrium structure at a precise temperature is a challenge that force fields often fail to overcome. Wang et al. highlighted the shortcoming of some of the most popular protein force field in predicting the temperature dependence of protein structural ensembles.<sup>36</sup> It is possible that our membrane system, simulated at 300K, does not fully represent the true structure at 300K. Lowering the temperature to 280K helped us to better resolve R-spots.

Evidence strongly suggests that the R-spots signal is not a result of alkane chain tilt. Previous literature has attributed the spots in this particular WAXS pattern as the product of tilted alkane chains.<sup>13</sup> We measured the tilt angle of the alkane chains of the 280K system and showed that it equilibrates to an average tilt angle of -2°(Fig. 7b), far from the 37°tilt angle previously used to explain R-spots.

To understand the most likely origin of R-spots, we determined which atoms gave rise to the feature. By removing all non-tail atoms from the trajectory and simulating a diffraction pattern with the remaining atoms, we were able to isolate the cause of the spots to the tails (Figure 7c). Since the tails stay nearly flat, we plotted their centroids (Figure 7d) and measured the angle between each centroid and its nearest neighbors with respect to the plane of the membrane. We see distinct peaks in the distribution of these angles (Figure 7).

The peaks in the nearest neighbor angle distribution are consistent with the location of R-spots. The peaks of interest in Figure 7e are located at  $\pm 33^\circ$  which is the same location where the highest intensity of spots are located in the simulated patterns. We confirmed this by radially integrating the 2D WAXS pattern for  $|q|$  values between 1.4 and 1.57 (between 4 and 4.5 Å in real space). We observe distinct peaks ca. 30°, in close agreement with the previously measured angle distribution (Figure 7f). We performed the same integration on the raw experimental data and found the angle at which R-spots reaches its highest intensity to be  $\pm 37^\circ$  which is a reconcilable difference with our simulated results.

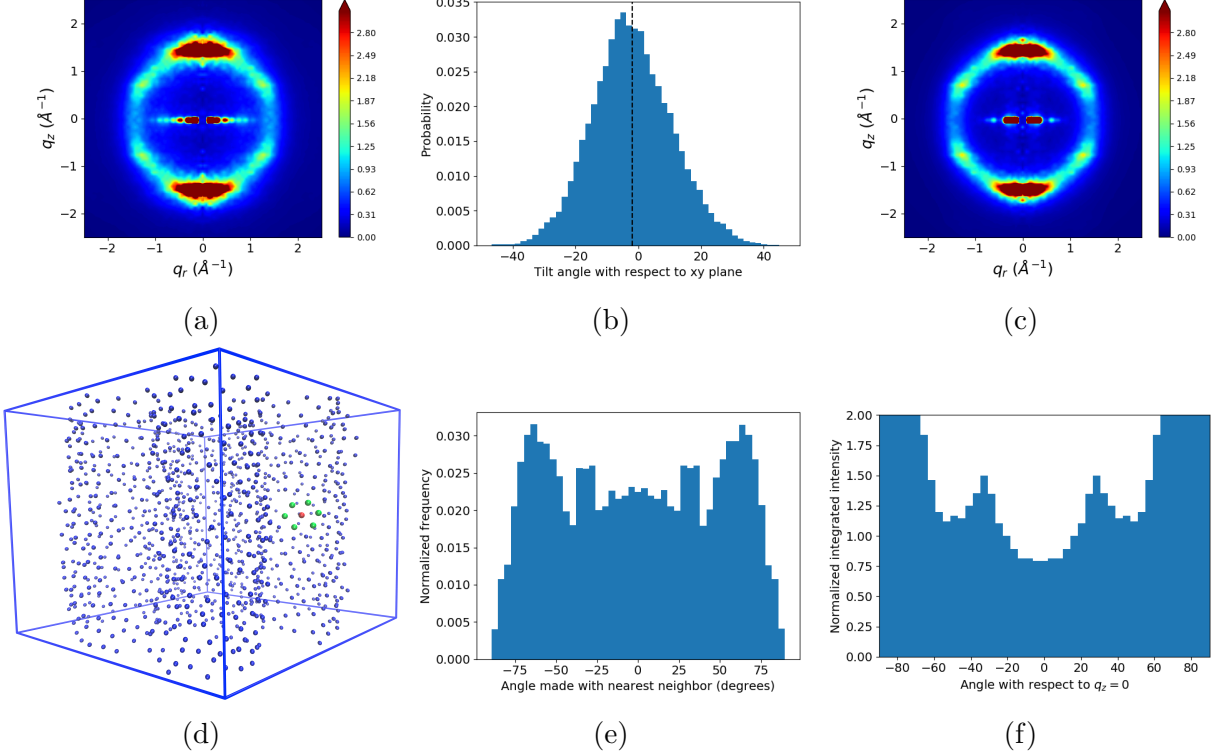


Figure 7: (a) R-spots increases in intensity when the temperature of the system is lowered to 280K. (b) We measured the average angle made between each monomer alkane tail and the membrane plane. The average tilt angle (dashed line) is near  $-2^\circ$  which is far from the  $37^\circ$  tilt angle previously used to explain R-spots. (c) To isolate the main cause of R-spots, we removed all atoms from the trajectory except for carbon atoms that constitute the tails. The simulated XRD pattern of the tails-only trajectory still shows R-spots. (d) Since the tails stay relatively flat, we plotted the centroid of each tail and observed that they pack hexagonally (for example, green colored centroids in the plot surround the red centroid in hexagonal fashion). (e) We hypothesize that R-spots is the result of ordered tail packing. Defining the membrane plane to be  $0^\circ$ , we measured the angles between each alkane chain tail centroid and its nearest neighbor centroids for the equilibrated sandwiched configuration simulated at 280K. Peaks that appear in each distribution are centered near  $\pm 33^\circ$ . (f) We radially integrated the simulated XRD patterns of the parallel displaced and sandwiched configuration within the region bounding R-alkanes. Peaks appear in the same location as the angle distributions which corroborates our hypothesis.

### 3.2.2 Discrepancies between experimental and simulated R- $\pi$

R- $\pi$  is more intense relative to the experimental system. The difference in intensity ranges from 3 times too high in the ordered parallel displaced system to 15 times too high in the ordered sandwiched configuration (Table 1).

The full width at half maximums (FWHM) of the  $q_r$  and  $q_z$  cross-sections of R- $\pi$  are broader than experiment (Figure 8). The FWHM of the  $q_z$  cross-section is 76 % larger than experiment and the  $q_r$  cross-section FWHM is 21% larger than experiment. Note that the experimental data is best fit with a Lorentzian function while the simulated patterns are best fit using a Gaussian function. The simulated spectra do not incorporate the effects of finite domain sizes, pressure broadening and instrumental broadening which would alter the peak shape. In the absence of these and other peak broadening effects, the experimental peak would actually be narrower, further increasing the discrepancy with simulation.

We have identified a number of potential ways that simulation conditions, forcefield and initial configurations could affect the intensity of R- $\pi$  as well as its FWHM in the  $q_z$  and  $q_r$  directions. We assessed each using a simplified model. Our simplified model represents each monomer head group as a single point and places them in either a parallel displaced or sandwiched configuration. We chose to explore the influence of thermal noise in each dimension, the effect of  $z$ -direction distance correlations between scatterers within columns, as well as correlation between columns since these are the variables we believe have the largest influence on peak shape and intensity.

As a baseline, we created a simplified model using the same amount of disorder present in our atomistic simulations. There are two sources of disorder to consider: thermal motion of atoms and quenched disorder which is created by rapid structural rearrangement during early equilibration and is largely locked into place for the remainder of the simulation. The latter has important implications for the reproducibility of this work since both initial configurations and velocity randomization at the beginning of equilibration can lead to different quenched configurations. We measured thermal disorder by calculating the standard deviation of the distribution of head group center of mass positions from their average positions. We measured quenched disorder by calculating the standard deviation of the distribution of head group center of masses from their idealized average positions. In the  $z$ -direction, we measured the deviation of the head group center of masses from an equally spaced column

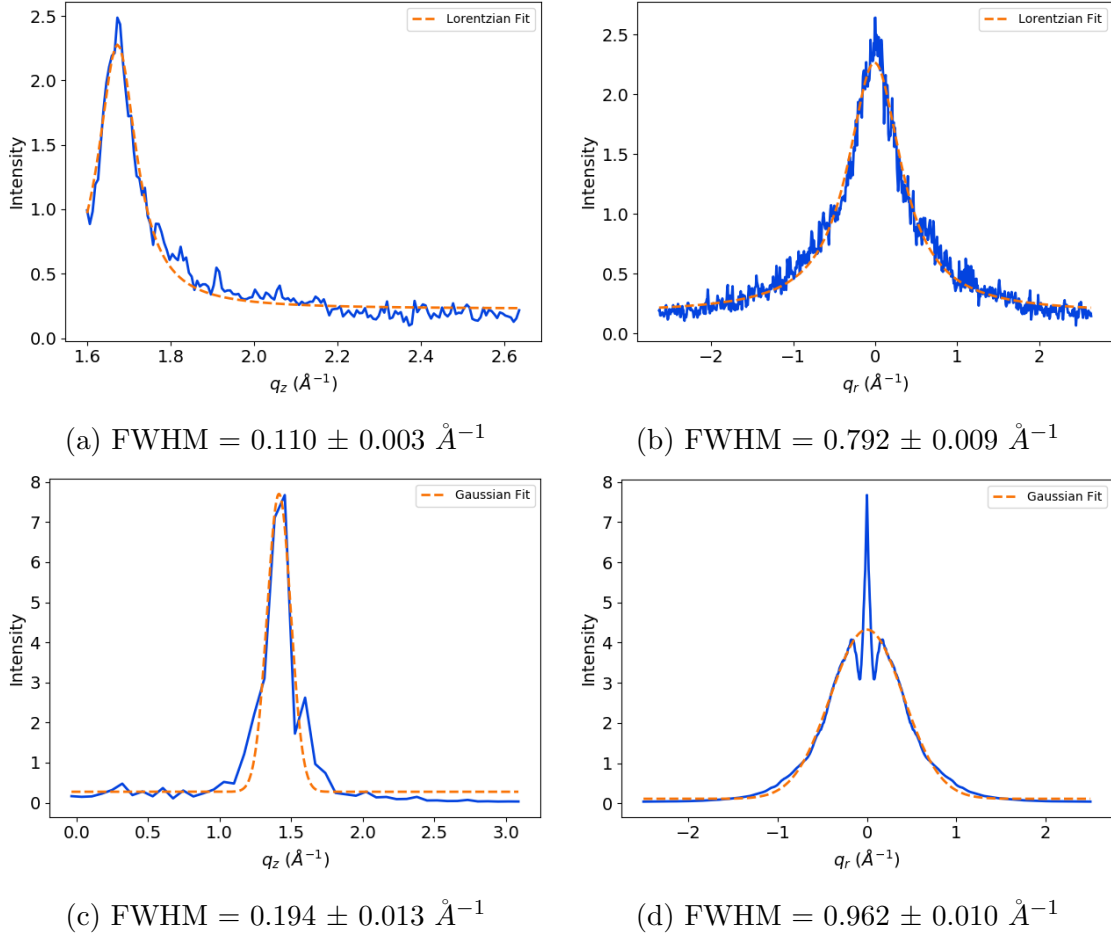


Figure 8: In experiments ((a) and (b)), (a), R- $\pi$  broadens in the  $q_z$  direction with a FWHM of  $0.110 \pm 0.003 \text{ \AA}^{-1}$  when fit with a Lorentzian function. (b) R- $\pi$  broadens in the  $q_r$  direction with a FWHM of  $0.792 \pm 0.009 \text{ \AA}^{-1}$  when fit with a Lorentzian function. In our simulations ((c) and (d)), (c) the FWHM of R- $\pi$  in the  $q_z$  direction is  $0.194 \pm 0.013 \text{ \AA}^{-1}$  when fit with a Gaussian function, nearly twice the width of experiment. (d) The simulated FWHM in the  $q_r$  direction is  $0.962 \pm 0.01 \text{ \AA}^{-1}$  when fit with a Gaussian function, about 20 % larger than experiment. Note that the large spike in the center is not included in the fit.

of head groups. In the  $xy$  plane, we calculated the deviation in radial position from the pore center and the angular deviation from equally spaced points surrounding the pore center. The values measured for each system and type of disorder are given in Table 2.

The intensity of  $R-\pi$  can be calculated from a single trajectory of uncorrelated configurations rather than as the average of multiple correlated trajectories. Theoretically, in order to mimic the simulated system, we should build an initial configuration which has the same amount of quenched disorder as our simulations and then create a trajectory to which we add thermal disorder to the initial configuration in order to create each frame. The average  $R-\pi$  intensity of 40, 100 frame trajectories created in this way was  $16.0 \pm 4.9$ . If instead we create a single trajectory from 1000 initial configurations, the intensity of  $R-\pi$  is 16.42, in close agreement with the mean of 40 simulations. We use the latter method for the remainder of this work since we can extract the trends we need using a single trajectory at a fraction of the computational cost.

When we simulated the diffraction pattern of a simple system trajectory of 1000 independent configurations, each created using the parameters for thermal and quenched disorder in order to place points, the  $q_r$  and  $q_z$  profiles of  $R-\pi$  are characterized by sharp peaks. We made this simple system, and all to follow, 4 times taller in the  $z$ -direction in order to access higher  $q_z$  resolution. Figure 9a and 9c shows the  $q_y$  and  $q_z$  cross-sections of  $R-\pi$  generated by simulating the structure factor of the trajectory. The distance between peaks in the  $q_y$  cross-section is equal to the distance between pores in real space.

**Table 2:** Deviation of the positions of the center of mass of head groups from their average positions (Thermal Disorder) as well as their idealized positions (Quenched Disorder) to use as simulated disorder into our model system.

System	Thermal Disorder			Quenched Disorder		
	$\sigma_x$ ( $\text{\AA}$ )	$\sigma_y$ (rad)	$\sigma_z$ ( $\text{\AA}$ )	$\sigma_z$ ( $\text{\AA}$ )	$\sigma_\theta$ (rad)	$\sigma_r$ ( $\text{\AA}$ )
Ordered Sandwiched	0.31	0.33	0.34	1.48	0.43	2.30
Ordered Parallel Displaced	0.51	0.52	0.30	1.45	0.43	2.28
Disordered Sandwiched	0.41	0.57	0.32	1.58	0.43	2.93
Disordered Parallel Displaced	0.39	0.31	0.33	1.65	0.43	2.63

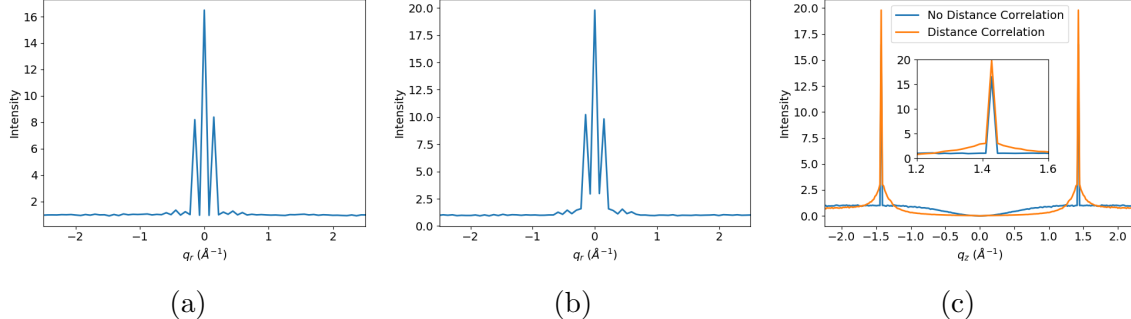


Figure 9: We generated X-ray diffraction patterns for simplified systems consisting of points meant to represent monomer head groups. We added a similar amount of noise to that seen in our simulations. (a) We added Gaussian noise to each particle in the  $z$ ,  $\theta$  and  $r$  directions. The  $q_y$  cross-section of R- $\pi$  contains three sharp peaks. (b) When we correlate the distance between points within each column, the intensity of R- $\pi$  increases but the sharp peaks remain with the same ratio of intensity between the center and outer peaks. (c) Correlation of the distance between scatterers in the  $z$ -direction causes R- $\pi$  to broaden in the  $q_z$  direction.

The distances between scatterers within each column are correlated with each other. In the simplified system described above, we added Gaussian noise to the mean positions of an equally spaced column of points. This ignores any interaction head groups might have with each other. To remedy this, we drew random samples from a multivariate normal distribution defined by the mean positions of an equally spaced column of points. We gave the distribution at each point along the column the same standard deviation,  $\sigma_z$ , shown in by Table 2. We defined a covariance matrix such that the covariance,  $v$ , in the distance,  $z$ , between scatterers decays exponentially from  $v$  according to the equation  $ve^{-z/L}$ , where  $L$  is the correlation length. Experimentally, the correlation length can be estimated as the inverse of the FWHM of the  $q_z$  cross-section of R- $\pi$ . Accordingly, the correlation length of the experimental system is  $\geq 9 \text{ \AA}$ . The value may be larger since the peak is likely broadened for a variety of other reasons. We simulated the structure factor of a simple system built as described above with a correlation length of  $30 \text{ \AA}$ . We chose  $30 \text{ \AA}$  in order to exaggerate the effect of correlation length for visual purposes. Subsequent structure factor calculations are all done with a correlation length of  $9 \text{ \AA}$ . The shape of the  $q_y$  cross-section (Figure 9b) remains the same while the the  $q_z$  cross-section (Figure 9c) broadens, as seen

in experiment. Additionally, there is a near 20 % increase in the maximum intensity of R- $\pi$  when the distances between scatterers are correlated.

The correlation length of vertically stacked scatterers in our simulations are in reasonable agreement with experiment. Since it is not feasible for us to simulate membranes with much taller columns for increased  $q_z$  resolution, and because the peak shape is convoluted by the extremely intense maximum of R- $\pi$ , we measured correlation length by plotting the one-dimensional pair distribution function,  $g(z)$ , for the centers of mass of monomer phenyl rings (Figure 10).

**Table 3: The correlation length is larger for systems in the ordered basin. The equilibrated vertical stacking distance,  $d_{equil}$ , is also smaller.**

System	$d$ (Å)	$d_{equil}$ (Å)	Correlation Length (Å)
Sandwiched	3.7	$4.27 \pm 0.03$	$4.2 \pm 0.8$
Parallel Displaced	3.7	$4.33 \pm 0.04$	$14.5 \pm 1.3$
Sandwiched	5.0	$4.48 \pm 0.07$	$3.2 \pm 0.9$
Parallel Displaced	5.0	$4.60 \pm 0.08$	$< d_{equil}$
Experiment	–	3.70	$10 \pm 1$

Monomers in the ordered basin stack closer together than those in the disordered basin (Table 3). We calculated the equilibrated vertical distance,  $d_{equil}$ , between monomers using Equation 3. Monomers in the ordered basin stack ca. 0.2 and 0.3 Å closer than those built in the disordered basin in the sandwiched and parallel displaced configurations respectively. The distance between stacked monomers is greater than experiment by 0.5–0.9 Å across all cases, with disordered basins at the high part of that range, 0.2 and 0.3 Å more distant. This behavior is not surprising since GAFF models atoms as point charges and does not appropriately model the aromatic  $\pi - \pi$  interactions which would make it more energetically favorable for the monomers to stack closer together. Additionally, it is possible that the tails prevent close stacking of monomer head groups and we do not achieve the timescales necessary for them to rearrange into a necessarily more tightly packed configuration. Since ordered basin systems pack closest together, they are likely the best choice for transport

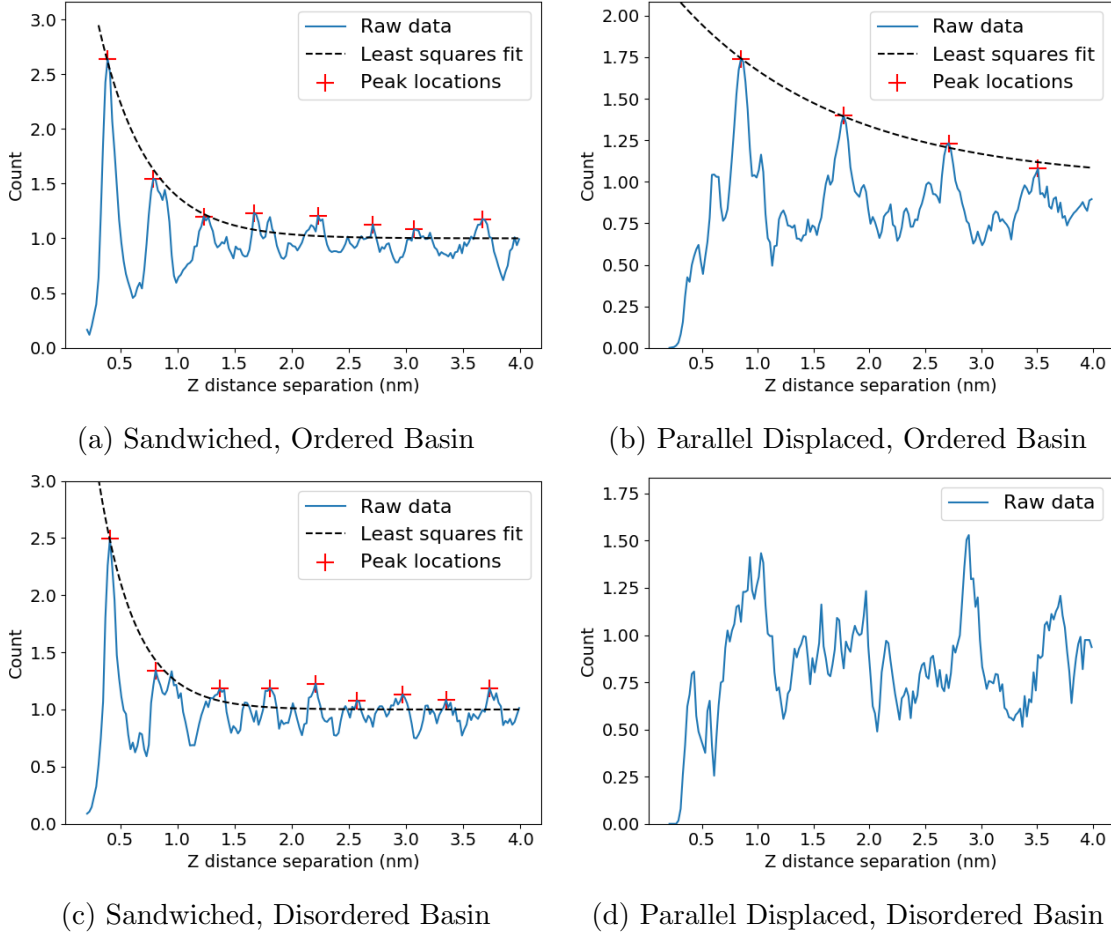


Figure 10: 1D correlation functions of the center of masses of aromatic head groups,  $g(z)$ , show decaying oscillatory behavior. We calculated the correlation length by fitting a decaying exponential function (Equation 2) to the peaks of  $g(z)$ . The correlation length is longer for ordered basin systems (Table 3). We did not attempt to calculate the correlation length for (d) because there are no clear peaks. We assume that its correlation is less than the vertical distance between monomers.

studies.

The correlation length of the parallel displaced, ordered basin system shows the closest agreement with experiment (Table 3). We calculated the correlation length of each system using Equation 2. We could not extract a reliable correlation length from the disordered parallel displaced configuration since the peaks do not show clear patterns that can easily be fit to an exponential decay. The correlation length of both sandwiched systems is relatively low because the height of the first peak of  $g(z)$  is so high. The peak height indicates the

degree of local ordering and influences the intensity of R- $\pi$ . If vertically adjacent sandwiched head groups were less ordered, which might be achieved with much longer simulations, then the leading peak intensity should decrease and the correlation length would increase. We expect that the leading peak would only get more intense if monomers stacked 3.7 Å apart. Conversely, parallel displaced head groups are not as confined by their vertically adjacent neighbors. This z-direction translational freedom may still be feasible if monomers stack 3.7 Å apart in a parallel displaced configuration, meaning the system would maintain a correlation length and R- $\pi$  intensity in relative agreement with experiment.

Increased thermal noise in the  $z$ -direction causes a drop in the intensity of R- $\pi$ , however the  $q_r$  profile remains unchanged. When we increase the thermal noise in the  $z$ -direction by 12% and 27%, we see a 3 and 15-fold decrease in the maximum intensity of R- $\pi$  respectively (Figure 11). Despite the decrease in intensity, the 3 cross-sections have the same shape (Figure 11b, whose sharp Bragg-like peaks are not consistent with experiment).

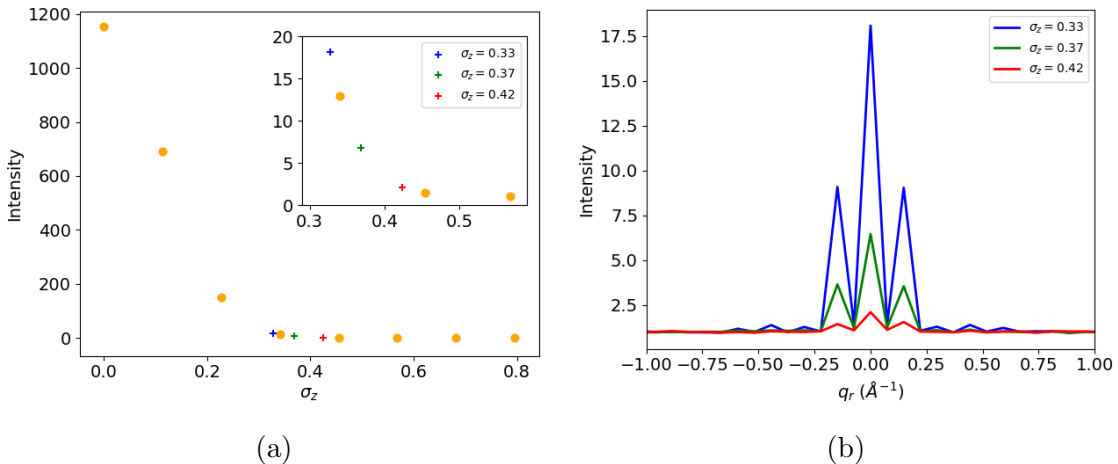


Figure 11: We can decrease the maximum intensity of R- $\pi$  by increasing thermal noise in the  $z$ -direction, however the  $q_r$  cross-section profile does not change. (a) The intensity of R- $\pi$  drops precipitously as we increase  $\sigma_z$ . We can decrease the intensity of R- $\pi$ , relative to the background intensity as seen in our simulation (blue) by a factor of 3 when we increase  $\sigma_z$  by 12% (green) and by a factor of 15 when we increase  $\sigma_z$  by 27 % (red). (b) Although the maximum intensity of R- $\pi$  decreases with increasing  $\sigma_z$ , the peak shape remains the same.

When we allow monomer columns to move independently in the  $z$ -direction, the intensity of R- $\pi$  drops and the  $q_r$  cross-section of the simulated diffraction patterns smooths out. We

created simple systems with varying amounts of association between columns. In the low limit, the center of mass of columns are situated at the same  $z$ -coordinate. This is how all simple systems have been created up to this point. We allow increasing independence of columns by randomly shifting each column in the  $z$ -direction using a uniform distribution bounded by  $(0, f \times d_{equil})$  where  $f$  ranges between 0 and 1. We limit this discussion to the sandwiched configuration since it is not feasible for columns in the parallel displaced configuration, as we have set them up, to move past each other. The trends seen above apply to both the sandwiched and parallel displaced systems. Allowing columns to move independently smooths out the  $q_r$  cross-section (Figure 12). Any amount of dependence results in sharp peaks. The intensity of R- $\pi$  decreases with increasing column independence. We see an 8-fold decrease in the intensity of R- $\pi$  when  $f = 1$  versus when  $f = 0$ .

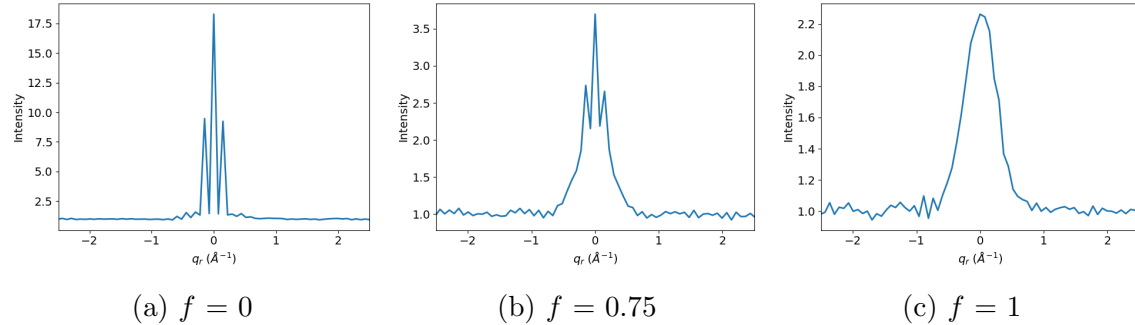


Figure 12: As we increase column independence using the  $f$  parameter, the intensity of R- $\pi$  decreases and the  $q_r$  cross-section of the simulated diffraction pattern becomes more smooth. (a) When we place all columns at the same  $z$  coordinate,  $f = 0$ , the intensity of R- $\pi$  is 18.3 and is characterized by sharp Bragg-like peaks. (b) When columns have a moderate amount of independence,  $f = 0.75$ , the intensity of R- $\pi$  decreases 5-fold to 3.7. The edges of the peak are beginning to smooth out, but sharp peaks still exist. (c) When columns are completely independent,  $f = 1$ , the intensity of R- $\pi$  decreases 8-fold to 2.3 and the cross-section is relatively smooth.

Increasing thermal noise in the  $xy$  plane causes the FWHM of the  $q_r$  cross-section of R- $\pi$  to decrease. We modified the disorder in both the  $r$  and  $\theta$  directions by multiplying their values by a factor of 0.5 and 2 (Figure 13). When we cut the noise in half, the FWHM increases by 88 %. When we double the noise, the FWHM decreases by 51 %.

We can use what we learned above in order to construct a better model, however there

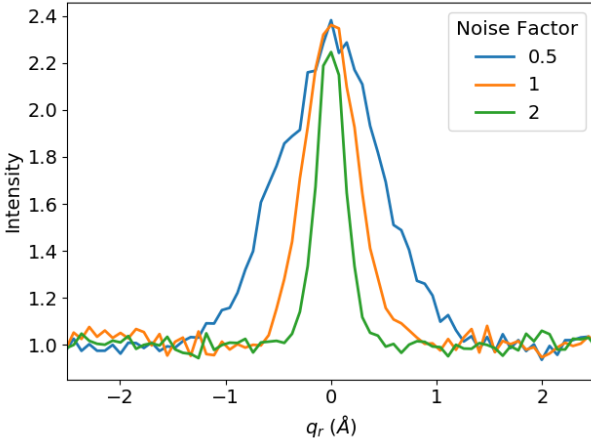


Figure 13: Increasing the amount of disorder in the  $xy$  plane decreases the FWHM of the  $q_y$  cross-section of R- $\pi$ . When we cut the amount of  $r$  and  $theta$  disorder in half (Noise factor = 0.5), the FWHM increases by 88%. When we double the disorder (Noise factor = 2), the FWHM decreases by 51%.

will still be shortcomings. We can decrease the intensity of R- $\pi$  if we incorporate more  $z$ -directional noise, which may come from increasing the system's temperature. We can adjust the parameters for aromatic carbons so that head groups stack more closely together. Perhaps the simplest thing to do is to create initial configurations whose columns are displaced randomly in the  $z$ -direction in order to mimic independence. Ultimately, we will need extremely long simulation times so that monomers within columns can rearrange and sample enough independent configurations to generate a robust simulated XRD pattern.

The architecture of each column is likely somewhere between sandwiched and parallel displaced. The parallel displaced configuration that we have simulated in this paper is an exaggerated manifestation of the parallel displaced  $\pi - \pi$  stacking mode. The simulated XRD pattern shows faint off-axis features at the same  $q_r$  value as R-double which is only in patterns generated from parallel displaced configurations. The monomers may prefer to be parallel displaced, but their displacement is likely only slightly shifted, on the  $xy$  plane, from the center of mass of their vertically adjacent neighbors. In this way, columns can more easily act independently while maintaining a parallel displaced structure.

The system size in the  $z$ -direction does not significantly alter the intensity of R- $\pi$ . We

equilibrated a sandwiched system with twice as many monomers per column so that the system size doubled in the z-direction. The correlation length increases modestly from  $4.5 \pm 0.4$  to  $7.3 \pm 1.2$  Å, and the intensity of R- $\pi$  decreases from 44.0 to 39.4. Visually, the correlation functions are nearly identical (See Figure S-27).

### 3.2.3 Origin of R-double

The appearance of R-double implies a vertical modulation in electron density every 7.4 Å. We are not able to achieve such modulation using our simple initial configurations. Although the position of monomers in parallel displaced configurations alternate every other layer, we know that such a helical configuration will not produce R-double, but only off-axis reflections at the same  $q_z$  value.<sup>37</sup> There is not a unique solution that describes the origin of R-double. Extracting the exact relationship between a diffraction pattern and its real space configuration is well-known as the phase problem.<sup>38</sup> We have proposed configurations that result in the appearance of R-double below, and we can speculate which makes the most physical sense. We explore both dry and wet configurations.

We can produce R-double if we rotate monomers with respect to vertically adjacent monomers. In this configuration, monomers are rotated so that the vector created by the bond extending from the carboxylate carbon to the phenyl ring is oriented  $\pm 15^\circ$  with respect to the vector extending from the carboxylate carbon to the pore center (Figure 14b). Every other monomer layer is rotated  $+15^\circ$  and those in between are rotated  $-15^\circ$ . This configuration allows monomer tails to sit between adjacent monomer tails which may be the most favorable way for them to pack. This configuration is stable short-term while unrestrained however R-double quickly fades after a few nanoseconds of simulation. The long-term stability of a configuration similar to this may be feasible if monomers stay stacked 3.7 Å apart.

We can also produce R-double if layers are not uniformly spaced. Rather, monomers might form pairs that stack less than 3.7 Å apart, and whose center of masses are spaced 7.4 Å from the next pair of monomers (Figure 14a). To our knowledge, there have been

no studies that specifically address the possibility of a configuration like this. Our force field causes our system to tend towards uniformly spaced layers. Simulations of unevenly spaced systems are only stable if position restraints are applied to heavy atoms of the phenyl rings. There is little evidence from QM studies of stacked  $\pi - \pi$  systems that this behavior is incorrect. ??

Adding water to the system appears to facilitate the appearance of R-double, through the creation of hydrogen bonding of water to carboxylate groups of consecutive layers. We added water to the parallel displaced and sandwiched configurations in the ordered basin and equilibrated them according to the wet equilibration procedure. There is no experimental measurement of water concentration in these membranes so we tested a range of water concentrations from 1% to 5%. R-double appears transiently in the simulated XRD pattern of the parallel displaced configuration with 1 wt% water (Figure 14c). It is not initially present, but appears after 200 ns of simulation time. After 450 ns, it disappears again. Simulated XRD patterns of all other solvated systems tested are shown in Figure S 24, however R-double is not present.

R-double appears in the solvated system due to the structure of the head groups. To demonstrate this, we removed the head groups from the trajectory used to produce Figure 14c in order to produce that shown in Figure 15a. R-double does not appear without the influence of the head groups. Water molecules must play a role in the structuring of the head groups since R-double does not appear in any dry simulations.

When two vertically stacked monomer head groups hydrogen bond with a shared water molecule, the monomers are drawn closer together (as illustrated in Figure 15b), which creates an asymmetry that allows R-double to appear. If a monomer head group shares a hydrogen bonded water molecule with a head group above itself, it will be less likely to share a water molecule with a head group below it due to steric constraints. The monomer head group below can just as easily share a water molecule with a head group below itself. In this scenario, the centers of each pair are 2 times the  $\pi$ -stacking distance apart which would

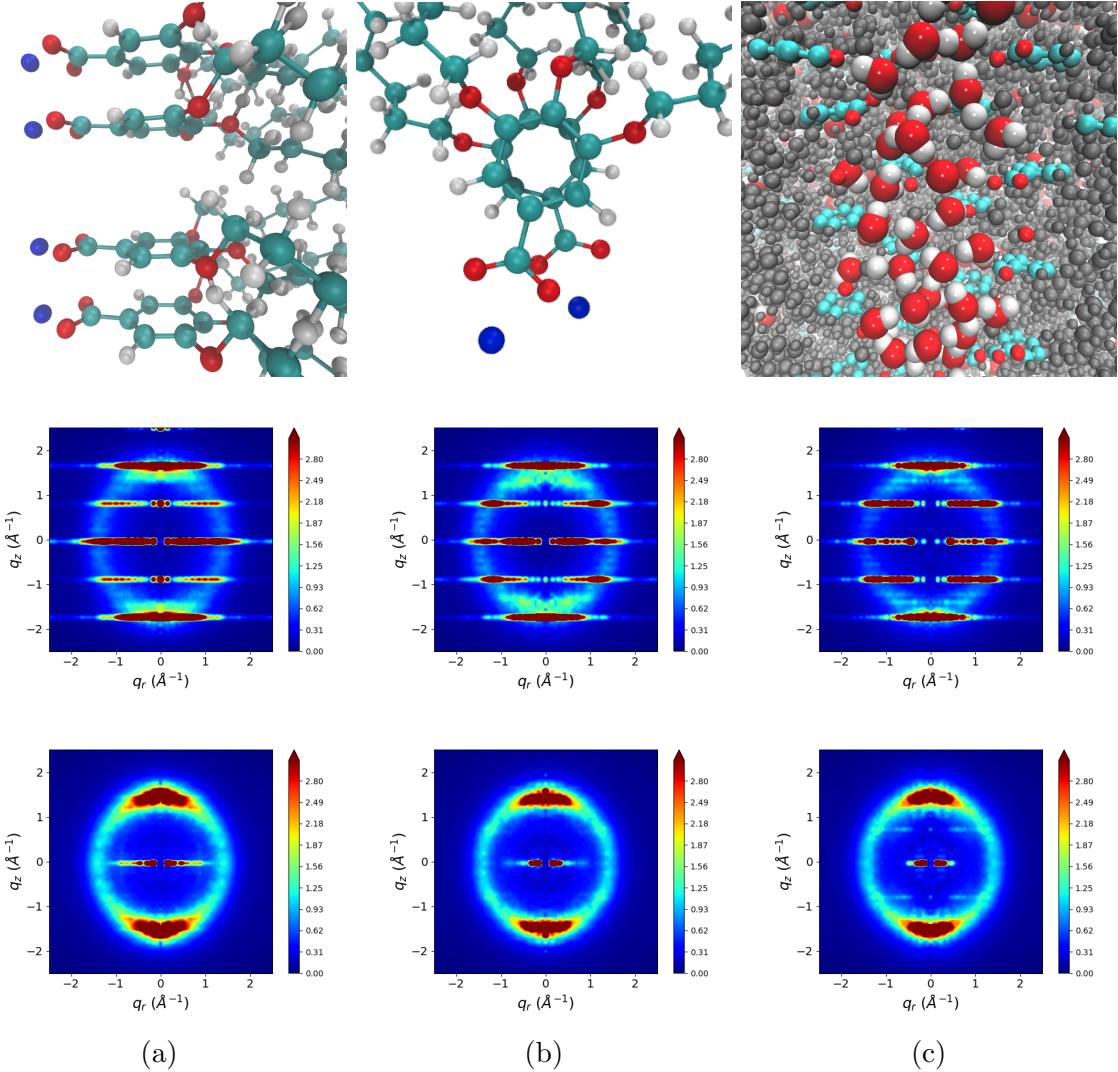


Figure 14: (a) When monomers are non-uniformly spaced (top), R-double appears if all heavy atoms of the head groups are held in place with position restraints (middle). R-double quickly fades once the position restraints are released (bottom). (b) When monomer head groups are rotated with respect to vertically adjacent monomers (top), R-double is visible while the heavy atoms of the head groups are held in place with position restraints (middle). Again, R-double fades once the position restraints are released. (c) When we add 1 wt% water to the parallel displaced configuration in the ordered basin (top) R-double is not initially present during the restrained portion of equilibration (middle). After 200 ns of equilibration, R-double becomes visible and persists for another 200 ns (bottom).

lead to R-double (much like the configuration in Figure 14a). There are a modest number of occurrences of this scenario, shown in Figure 15c. Peaks in the distributions represent the scenario where a monomer head group shares a water molecule with a head group vertically above it. In Figure 15d, we calculated the discrete Fourier transform of the distributions

which we used as a rough indicator of whether the head group arrangement will lead to R-double. We see the strongest indicator of asymmetric monomer stacking in Pore 1 where the peaks at  $0.5 \text{ layers}^{-1}$  are clearly distinguished, meaning there is periodicity every two layers.

It is thus most likely that R-double originates from water molecules as described above, as it is the only mechanism that can be observed without externally restraining positions. The extent of the hydrogen bonding network that forms is largely determined by the accuracy of the forcefield. It is possible that a more realistic forcefield would make the effect stronger or weaker. If this is truly the mechanism, it implies that the system studied by Feng et al.<sup>13,15</sup> was not truly a thermotropic Col<sub>h</sub> phase. Rather, they were very low water content H<sub>II</sub> phases unintentionally created due to the neat monomers' hydroscopicity. This detail may therefore be important for reproducing the results of Feng et al.

### 3.3 Atomistic structure of pore columns

We are most interested in the structure and composition of the pores since we would like to study transport mechanisms within them. We have shown that the tails possess a certain degree of order which is necessary in order to create the complex WAXS pattern shown experimentally, but they will not be involved in a separation process. We aim to further understand the pore architecture and observe the differences, if any, between the different equilibrated configurations studied so far.

In general, the composition of each region, particularly within our definition of the pore region, is similar between all systems. This suggests that the details of transport may be relatively independent of the structural differences between different possible structures studied here.

We plotted the number densities of heavy atoms in the head group, carbon atoms in the tail region and all sodium ions (Figure 16). For the head group region, we used heavy atoms making up the aromatic rings and carboxylate groups. For the tail region we used carbon

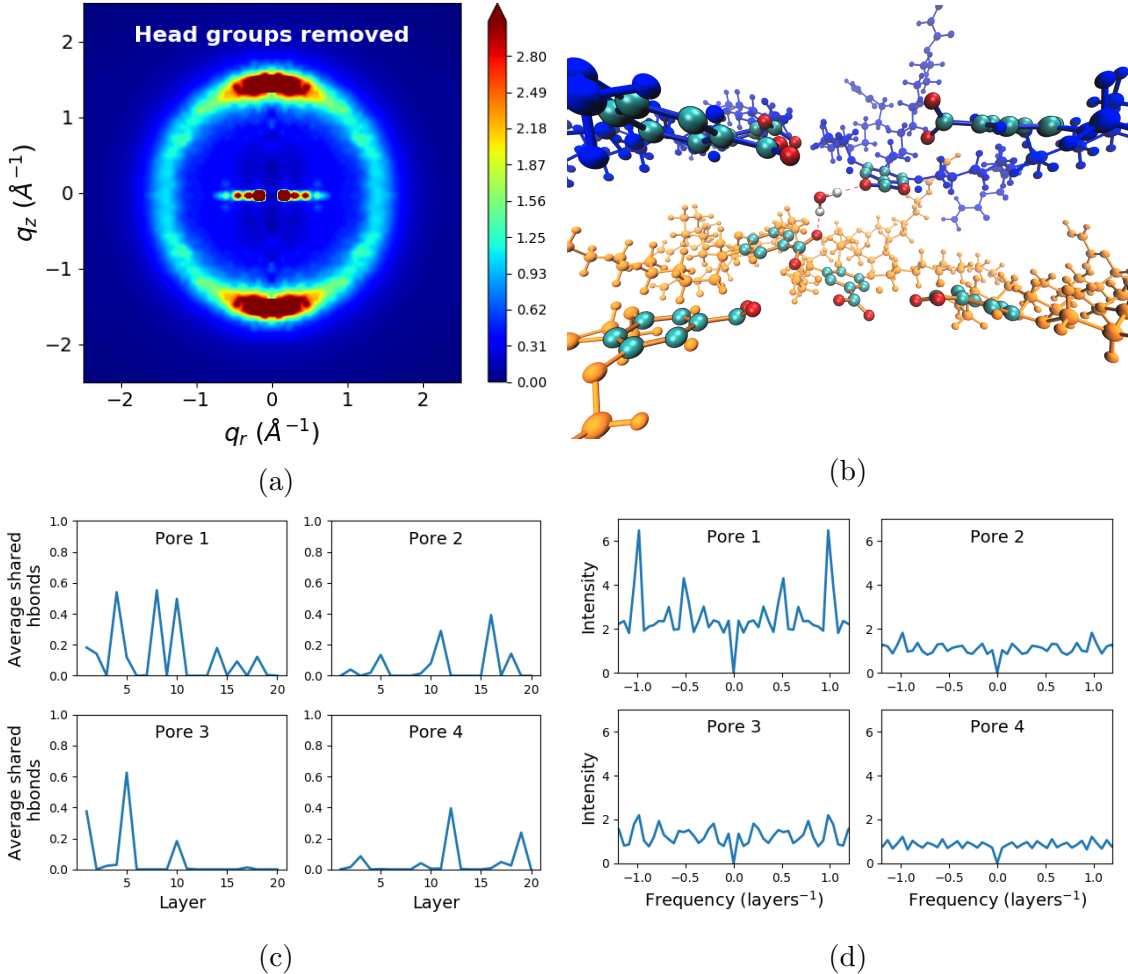


Figure 15: (a) The structure of the head groups is responsible for the appearance of R-double. When we remove head groups from the trajectory, the simulated diffraction pattern no longer shows R-double. (b) Monomer head groups above or below each other that hydrogen bond with a shared water molecule are drawn closer together. Blue monomers were stacked above orange monomers in the initial configuration. (c) Monomers in each column are numbered from 1–20. For simplicity, we define a layer to be composed of all same-number monomers. Peaks in the distributions indicate a shared hydrogen bonded water molecule between a monomer head group and one in the layer vertically above it. For example, in Pore 1, monomer 7 shares a hydrogen bond with a monomer in layer 8 (pictured in (b)). In this scenario, monomers are no longer evenly spaced in the z-direction since they are pulled closer together by hydrogen bonds. (d) We performed discrete Fourier transforms on each distribution in (c). In all cases, the strongest peak represents periodicity every layer. In Pore 1, there is also periodicity every other layer as indicated by the strong peak at  $0.5 \text{ layers}^{-1}$ . In this case, the center of mass of two adjacent pairs is separated by twice the average monomer stacking distance, while the four monomers involved are unequally spaced. These conditions may give rise to R-double.

atoms of the monomer tails (See Figure S-3 for a diagram). We averaged the histograms over at least 50 ns of equilibrated trajectory.

There is a gradient in pore composition transitioning radially from the hydrophilic to the hydrophobic region, rather than an abrupt division. Based on size-exclusion experiments, we define the pore radius to be 0.6 nm.<sup>8</sup> The system does not confine sodium ions and head groups to just within the pore region. For dry systems, 19% of sodium ions exist outside the pore region (except sandwiched, ordered basin, where 16% are outside the pore). Additionally, we see that in all cases, about 3% of the plotted tail density is located within the pore region (except ordered sandwiched, where 1.5% are within the pore region). For the solvated system, the results are similar, however the head group density is shifted slightly radially outward. This is likely due to swelling of the pore by water.

The space in the pore region is filled with a mixture of sodium ions and head groups. The distributions appear somewhat different near  $r=0$ , but that noise is expected since there is significantly less sampling as  $r$  approaches 0. Regardless, all systems, including the solvated system, have a significant number of head groups and sodium ions occupying the pore center. This observation highlights that the pore region is dense, not hollow, and may impede transport of solvent and solutes when compared to the previous idealized picture of a hollow tube conducive to transport.

### 3.4 Slow dynamics

We observe slow dynamics in our system. Typical diffusion constants for columnar liquid crystals have been reported to be between  $10^{-11} \text{ m}^2/\text{s}$ <sup>39</sup> and  $10^{-14} \text{ m}^2/\text{s}$ .<sup>40</sup> We measured the diffusion constants of monomers in each of the systems we studied (See Table S-2) and learned that they are all on the order of  $10^{-14} \text{ m}^2/\text{s}$ . This is not entirely surprising considering how densely the monomers are packed as implied by diffraction experiments. The entangled tails likely restrict both vertical and lateral movement.

Consequently, there is not enough movement on the timescales we simulated for the

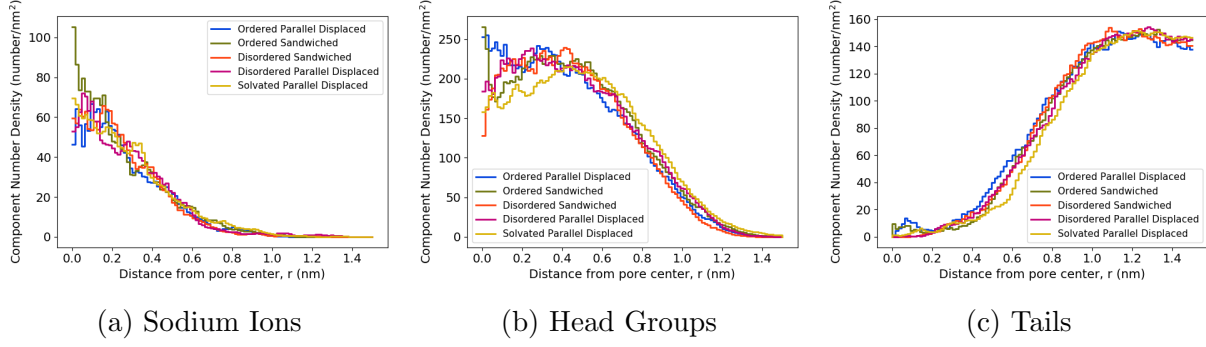


Figure 16: In all cases, the component radial distribution functions are similar. They exhibit a composition gradient transitioning from the hydrophilic to the hydrophobic regions. The biggest differences are at  $r=0$  where noise is expected to be high due to decreased sampling. The center of the pore is not hollow, but contains sodium ions and head groups, even when the system is solvated. This architecture may impede transport in the real system in a chemically-dependent manner. The solvated system has a lower density of head groups near the pore center which is likely due to the swelling that is necessary in order to fit water molecules in the pore region.

system to consistently reach a structure equivalent to experiment. In all cases our monomers equilibrate to a stacking distance that is too large compared to experiment. While this may be in large part due to the forcefield's inability to model aromatic interactions, it is also possible that the monomer tails do have enough time to pack as tightly as they could. More densely packed tails could allow the monomers to stack closer together.

We quantified the movement of the tails during our simulations by calculating the autocorrelation function of the dihedral angle formed around the bond between the head groups and the ether oxygens which attach the tails to the head group (See Figure S-4). We exclude the dihedral from the middle tail since it is fundamentally different than the two symmetric outside tails. We limited these studies to the sandwiched configuration for simplicity.

The ether dihedrals become decorrelated on a reasonable timescale when the temperature is raised. At 300K (Figure 17a), the autocorrelation function does not cross the x-axis until  $\sim 105$  ns meaning that tails fully rotate on average about times over the course of the 400 ns that we studied. Additionally, the correlation function plateau's near a value of -0.2 which indicates that the tails are starting in an unfavorable configuration. We implemented distance

restraints between the centers of mass of monomer head groups to preserve the hexagonal phase, then raised the temperature of the equilibrated 300 K ordered basin sandwiched system to 500 K. We witnessed decorrelation of the ether dihedrals after  $\sim$ 11 ns with a plateau at 0, (Figure 17b) indicating a complete loss of memory. We annealed the resultant configuration back down to 300 K over 200 ns to see if the increased rotational freedom might allow the system to relax into to a more tightly packed configuration.

Decorrelating the ether dihedrals at high temperature, followed by thermal annealing does not improve packing in our model. In the ideal case, if all monomers stacked  $3.7 \text{ \AA}$  apart, the z-dimension of our unit cell should be 7.4 nm. In the ordered basin, sandwiched system studied in this paper, the z-dimension of the unit cell equilibrated to 8.87 nm, which is roughly consistent with the stacking distance reported in Table 3. After 200 ns of annealing from 500K to 300K, the z-dimension of the unit cell was 9.22 nm. We repeated the annealing procedure over the course of 400 ns and the final z-dimension of the unit cell was 9.20 nm. Much longer annealing simulations may get the system to the correct density, but we do not have the resources to further explore this approach.

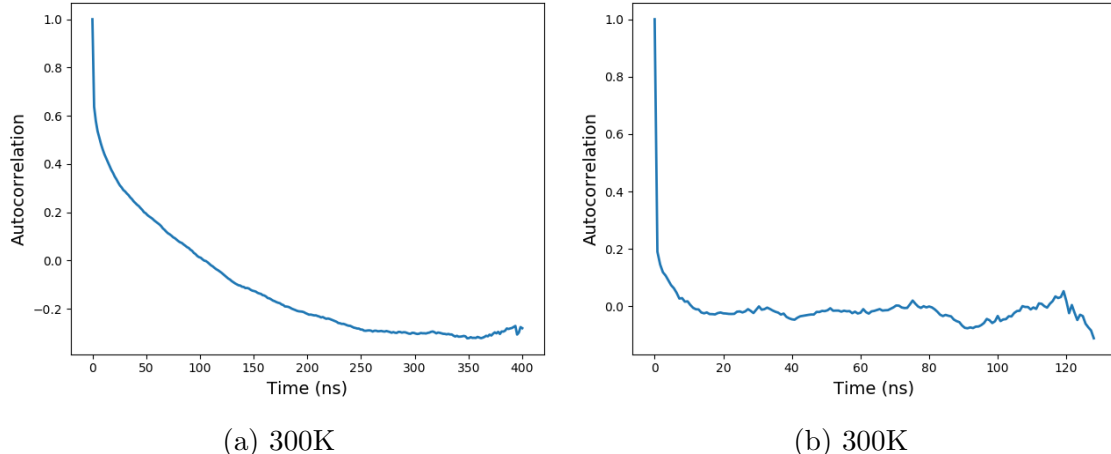


Figure 17

### 3.5 Ionic Conductivity Measurements

We calculated the ionic conductivity of the parallel displaced configuration in the ordered basin with 1 wt % water since we believe its structure is the closest match to experiment. Our model estimates the ionic conductivity within one order of magnitude of experiment (Figure 18). We verified the value calculated by the Nernst-Einstein relationship using the collective diffusion model<sup>41</sup> (See section S 26). The values calculated by the collective diffusion model agree with Nernst-Einstein values within error, however there is a much higher uncertainty that would require much longer simulations to lower.

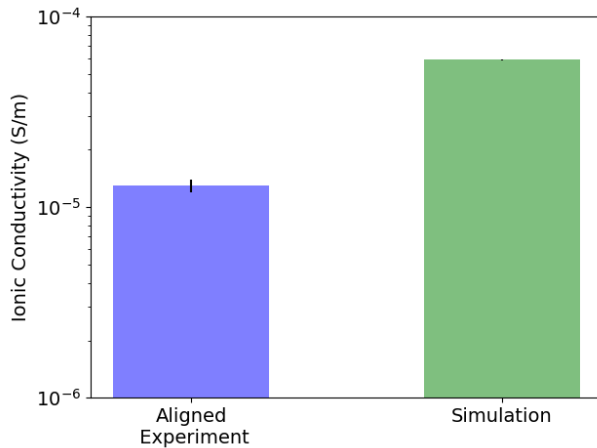


Figure 18: The calculated ionic conductivity of the simulated system is approximately one order of magnitude higher than experiment.

The calculated value of ionic conductivity is 5x higher than experiment because we simulated infinitely long, aligned pores. The ionic conductivity measurement to which we are comparing was done with a 80  $\mu\text{m}$  thick film, nearly 10,000 times thicker than our simulated system. The thick film is likely imperfectly aligned and has defects leading to non-contiguous pores. It has been shown that there is a large dependence of ionic conductivity on the alignment of the pores. The ionic conductivity of an isotropically aligned film is ca. 85 times lower than that of the nearly aligned film to which we are comparing.<sup>13</sup> We hypothesize that a thin, perfectly aligned film would have a value of ionic conductivity in closer agreement with our model.

### 3.6 Effect of Cross-linking

Experimentally, membranes are crosslinked for mechanical stability before use. We applied our cross-linking algorithm to equilibrated sandwiched and parallel displaced configurations in the ordered pore basin. We allowed the cross-linking algorithm to propagate until greater than 90% of vinyl groups were either involved in a cross-linking reaction or were terminated (see section S-13 for further details of the cross-linking algorithm). We allowed the cross-linked configurations to simulate for 100 ns further in the NPT ensemble.

There are only minor changes to the physical characteristics of these systems when they are cross-linked (See Figure 19). The ionic conductivity of the sandwiched configuration decreases while that of the parallel displaced configuration stays the same. The pore spacing decreases in both systems by 0.07 nm. The vertical monomer stacking distance increases in the sandwiched configuration and decreases in the parallel displaced configuration, however the values of cross-linked configurations fall within uncertainty of their un-crosslinked counterparts. The correlation length decreases in both systems, but is most pronounced in the parallel displaced system.

## 4 Conclusions

We have used detailed molecular modeling of the  $\text{Col}_h$  phase formed by Na-GA3C11 in order to study its nanoscopic structure. While there have been efforts to model formation of various liquid crystalline phases with molecular dynamics, to our knowledge there have been no studies which attempt to examine their structure with the same level of detail presented here.

We observed a number of metastable configurations, stable for hundreds of nanoseconds, which do not fit the experimental profile we have tried to match. We explored two classes of metastable basins which are dependent on the initial vertical stacking distance between monomers: the ordered and disordered pore basins. We expect that these metastable con-

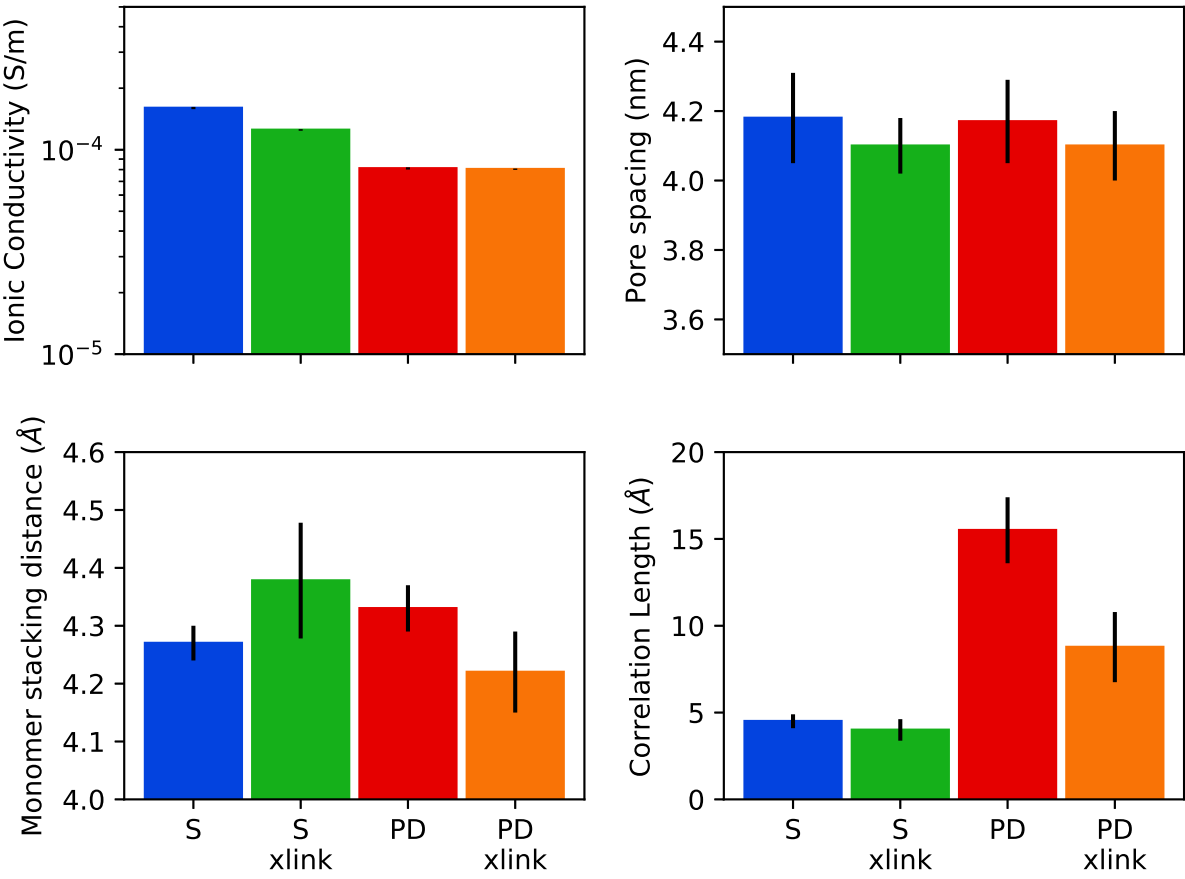


Figure 19: There are minor differences between the physical properties of a crosslinked (xlink) system versus an uncrosslinked system. The sandwiched configuration (S) exhibits a smaller decrease in its ionic conductivity, while the parallel displaced (PD) configuration remains constant. The pore spacing of both systems decreases upon crosslinking. The vertical distance between stacked monomers increases in the sandwiched configuration and decreases in the parallel displaced configuration. The correlation length decreases in both configurations.

figurations will eventually rearrange and converge to a single equilibrium structure. We conducted extensive analysis in order to isolate structures which most closely resemble the true equilibrium structure.

We achieve maximum structural consistency with experiment, as determined by simulated 2D XRD patterns, when we build our model in the ordered basin parallel displaced configuration with 5 monomer columns per pore and 1 wt% water. R-alkanes and R-pores appear where expected for the reasons originally predicted. We find that R-spots is likely

due to ordered alkane chain packing.  $R-\pi$  appears at lower  $q$  values than experiment because monomer stack too far apart. Finally, we observed that our model can only produce  $R$ -double when we add 1 wt% water to the system. This observation has possible implications for the reproducibility of the experimental results from Feng et al. since they claim that their membrane is completely dry.

We characterized the environment centered around the membrane pores and learned that the pores are generally filled with monomer head groups and sodium ions. All dry systems studied showed a similar distribution of sodium, head groups and tails while the wet system shows evidence of slight swelling, with minor changes in the distributions due to the presence of water molecules. We also observed that there is not a hard partition between hydrophilic and hydrophobic regions, rather there is a gradient. This finding has raised questions about the nature of size-exclusion separations in systems without a well-defined pore size, which potentially could give rise to separations that vary with chemical identity as well as size.

Our system can reasonably estimate ionic conductivity. Our calculations are about 1 order of magnitude higher than experiment, however that is to be expected since we are simulating a perfectly straight and defect-free membrane.

Finally, we verified that our conclusions do not change when the system is cross-linked by the algorithm we implemented. The diffraction pattern weakens relative to the uncross-linked system, the ionic conductivity drops by a factor of ca. 1.5, in closer agreement with experiment, the pore spacing decreases and the membrane becomes thicker; however, all changes are relatively minor, preserving most of the features well.

With the structural understanding gained by these simulations, it becomes possible evaluate transport of various solutes within the system, and apply the knowledge gained from this study in order to suggest improvements to the existing system as well as to evaluate new unsynthesized LLC systems.

## References

- (1) McCutcheon, J. R.; McGinnis, R. L.; Elimelech, M. A novel ammoniacarbon dioxide forward (direct) osmosis desalination process. *Desalination* **2005**, *174*, 1–11.
- (2) Dischinger, S. M.; Rosenblum, J.; Noble, R. D.; Gin, D. L.; Linden, K. G. Application of a lyotropic liquid crystal nanofiltration membrane for hydraulic fracturing flowback water: Selectivity and implications for treatment. *Journal of Membrane Science* **2017**, *543*, 319–327.
- (3) Xie, M.; Shon, H. K.; Gray, S. R.; Elimelech, M. Membrane-based processes for wastewater nutrient recovery: Technology, challenges, and future direction. *Water Research* **2016**, *89*, 210–221.
- (4) Werber, J. R.; Osuji, C. O.; Elimelech, M. Materials for next-generation desalination and water purification membranes. *Nature Reviews Materials* **2016**, *1*, 16018.
- (5) Gin, D. L.; Bara, J. E.; Noble, R. D.; Elliot, B. J. Polymerized Lyotropic Liquid Crystal Assemblies for Membrane Applications. *Macromolecular Rapid Communications* **2008**, *29*, 367–389.
- (6) Wijmans, J. G.; Baker, R. W. The solution-diffusion model: a review. *Journal of Membrane Science* **1995**, *107*, 1–21.
- (7) Smith, R. C.; Fischer, W. M.; Gin, D. L. Ordered Poly(p-phenylenevinylene) Matrix Nanocomposites via Lyotropic Liquid-Crystalline Monomers. *Journal of the American Chemical Society* **1997**, *119*, 4092–4093.
- (8) Zhou, M.; Kidd, T. J.; Noble, R. D.; Gin, D. L. Supported Lyotropic Liquid-Crystal Polymer Membranes: Promising Materials for Molecular-Size-Selective Aqueous Nanofiltration. *Adv. Mater.* **2005**, *17*, 1850–1853.

- (9) Donnan, F. G. Theory of membrane equilibria and membrane potentials in the presence of non-dialysing electrolytes. A contribution to physical-chemical physiology. *Journal of Membrane Science* **1995**, *100*, 45–55.
- (10) Hatakeyama, E. S.; Gabriel, C. J.; Wiesnauer, B. R.; Lohr, J. L.; Zhou, M.; Noble, R. D.; Gin, D. L. Water filtration performance of a lyotropic liquid crystal polymer membrane with uniform, sub-1-nm pores. *Journal of Membrane Science* **2011**, *366*, 62–72.
- (11) Hatakeyama, E. S.; Wiesnauer, B. R.; Gabriel, C. J.; Noble, R. D.; Gin, D. L. Nanoporous, Bicontinuous Cubic Lyotropic Liquid Crystal Networks via Polymerizable Gemini Ammonium Surfactants. *Chem. Mater.* **2010**, *22*, 4525–4527.
- (12) Carter, B. M.; Wiesnauer, B. R.; Hatakeyama, E. S.; Barton, J. L.; Noble, R. D.; Gin, D. L. Glycerol-Based Bicontinuous Cubic Lyotropic Liquid Crystal Monomer System for the Fabrication of Thin-Film Membranes with Uniform Nanopores. *Chem. Mater.* **2012**, *24*, 4005–4007.
- (13) Feng, X.; Tousley, M. E.; Cowan, M. G.; Wiesnauer, B. R.; Nejati, S.; Choo, Y.; Noble, R. D.; Elimelech, M.; Gin, D. L.; Osuji, C. O. Scalable Fabrication of Polymer Membranes with Vertically Aligned 1 nm Pores by Magnetic Field Directed Self-Assembly. *ACS Nano* **2014**, *8*, 11977–11986.
- (14) Matyka, M.; Khalili, A.; Koza, Z. Tortuosity-porosity relation in porous media flow. *Phys. Rev. E* **2008**, *78*, 026306.
- (15) Feng, X.; Nejati, S.; Cowan, M. G.; Tousley, M. E.; Wiesnauer, B. R.; Noble, R. D.; Elimelech, M.; Gin, D. L.; Osuji, C. O. Thin Polymer Films with Continuous Vertically Aligned 1 nm Pores Fabricated by Soft Confinement. *ACS Nano* **2016**, *10*, 150–158.
- (16) Resel, R.; Leising, G.; Markart, P.; Kriechbaum, M.; Smith, R.; Gin, D. Structural properties of polymerised lyotropic liquid crystals phases of 3,4,5-tris(\$mega\$-

- acryloxyalkoxy)benzoate salts. *Macromolecular Chemistry and Physics* **2000**, *201*, 1128–1133.
- (17) McIntosh, T. J.; Simon, S. A.; MacDonald, R. C. The organization of n-alkanes in lipid bilayers. *Biochimica et Biophysica Acta (BBA) - Biomembranes* **1980**, *597*, 445–463.
- (18) Govind, A. S.; Madhusudana, N. V. A simple molecular theory of smectic-C liquid crystals. *EPL* **2001**, *55*, 505.
- (19) Zhu, X.; Scherbina, M.; Bakirov, A.; Gorzolnik, B.; Chvalun, S.; Beginn, U.; Moller, M. Methacrylated Self-Organizing 2,3,4-Tris(alkoxy)benzenesulfonate: A New Concept Toward Ion-Selective Membranes. *Chem. Mater.* **2006**, *18*, 4667–4673.
- (20) Chaikin, P.; Lubensky, T. *Principles of condensed matter physics*, 1st ed.; Cambridge University Press, 1995.
- (21) Wang, J.; Wolf, R. M.; Caldwell, J. W.; Kollman, P. A.; Case, D. A. Development and testing of a general amber force field. *J. Comput. Chem.* **2004**, *25*, 1157–1174.
- (22) Wang, J.; Wang, W.; Kollman, P. A.; Case, D. A. Automatic atom type and bond type perception in molecular mechanical calculations. *Journal of Molecular Graphics and Modelling* **2006**, *25*, 247–260.
- (23) Case, D.; Betz, R.; Botello-Smith, W.; Cerutti, D.; Cheatham, T., III; Darden, T.; Duke, R.; Giese, T.; Gohlke, H.; Goetz, A. et al. AmberTools16. 2016.
- (24) Bekker, H.; Berendsen, H. J. C.; Dijkstra, E. J.; Achterop, S.; van Drunen, R.; van der Spoel, D.; Sijbers, A.; Keegstra, H.; Reitsma, B.; Renardus, M. K. R. Gromacs: A parallel computer for molecular dynamics simulations. *Physics Computing* **1993**,
- (25) Berendsen, H. J. C.; van der Spoel, D.; van Drunen, R. GROMACS: A message-passing parallel molecular dynamics implementation. *Computer Physics Communications* **1995**, *91*, 43–56.

- (26) Van Der Spoel, D.; Lindahl, E.; Hess, B.; Groenhof, G.; Mark, A. E.; Berendsen, H. J. C. GROMACS: Fast, flexible, and free. *J. Comput. Chem.* **2005**, *26*, 1701–1718.
- (27) Hess, B.; Kutzner, C.; van der Spoel, D.; Lindahl, E. GROMACS 4: Algorithms for Highly Efficient, Load-Balanced, and Scalable Molecular Simulation. *J. Chem. Theory Comput.* **2008**, *4*, 435–447.
- (28) Mondal, J.; Mahanthappa, M.; Yethiraj, A. Self-Assembly of Gemini Surfactants: A Computer Simulation Study. *J. Phys. Chem. B* **2013**, *117*, 4254–4262.
- (29) Martnez, L.; Andrade, R.; Birgin, E. G.; Martnez, J. M. PACKMOL: A package for building initial configurations for molecular dynamics simulations. *J. Comput. Chem.* **2009**, *30*, 2157–2164.
- (30) Sinnokrot, M. O.; Valeev, E. F.; Sherrill, C. D. Estimates of the Ab Initio Limit for Interactions: The Benzene Dimer. *J. Am. Chem. Soc.* **2002**, *124*, 10887–10893.
- (31) Chodera, J. D. A Simple Method for Automated Equilibration Detection in Molecular Simulations. *Journal of Chemical Theory and Computation* **2016**, *12*, 1799–1805.
- (32) Shirts, M. R.; Chodera, J. D. Statistically optimal analysis of samples from multiple equilibrium states. *The Journal of Chemical Physics* **2008**, *129*, 124105.
- (33) Kuriabova, T.; Betterton, M. D.; Glaser, M. A. Linear aggregation and liquid-crystalline order: comparison of Monte Carlo simulation and analytic theory. *J. Mater. Chem.* **2010**, *20*, 10366–10383.
- (34) Einstein, A. Investigations on the theory of the brownian movement. *Dover Publications* **1956**,
- (35) Watson, J.; Crick, F. A structure for Deoxyribose Nucleic Acid. *Nature* **1953**, *171*, 737–738.

- (36) Wang, L.-P.; McKiernan, K. A.; Gomes, J.; Beauchamp, K. A.; Head-Gordon, T.; Rice, J. E.; Swope, W. C.; Martnez, T. J.; Pande, V. S. Building a More Predictive Protein Force Field: A Systematic and Reproducible Route to AMBER-FB15. *J. Phys. Chem. B* **2017**, *121*, 4023–4039.
- (37) Harburn, G.; Taylor, C. A.; Welberry, T. R. *Atlas of optical transforms*; Cornell University Press, 1975; Google-Books-ID: BwCFAAAIAAJ.
- (38) Taylor, G. The phase problem. *Acta Cryst D, Acta Cryst Sect D, Acta Crystallogr D, Acta Crystallogr Sect D, Acta Crystallogr D Biol Crystallogr, Acta Crystallogr Sect D Biol Crystallogr* **2003**, *59*, 1881–1890.
- (39) Dong, R. Y.; Goldfarb, D.; Moseley, M. E.; Luz, Z.; Zimmermann, H. Translational diffusion in discotic mesophases studied by the nuclear magnetic resonance pulsed field gradient method. *J. Phys. Chem.* **1984**, *88*, 3148–3152.
- (40) Dvinskikh, S. V.; Fur, I.; Zimmermann, H.; Maliniak, A. Molecular self-diffusion in a columnar liquid crystalline phase determined by deuterium NMR. *Phys. Rev. E* **2002**, *65*, 050702.
- (41) Liu, Y.; Zhu, F. Collective diffusion model for ion conduction through microscopic channels. *Biophys. J.* **2013**, *104*, 368–376.

## Graphical TOC Entry

